REPORT DOCUMENTATION PAGE

Public reporting burden for this collection of information is estimated to average 1 hour per response, including the time for reviewing instructions, searching existing data sources, gathering and maintaining the data needed, and completing and reviewing the collection of information. Send comments regarding this burden estimate or any other aspect of this collection of information, including suggestions for reducing this burden, to Washington Headquarters Services, Directorate for information Operations and Reports, 1215 Jefferson Davis Highway, Suite 1204, Arlington, VA 22202-4302, and to the Office of Management and Budget, Paperwork Reduction Project (0704-0188), Washington, DC 20503.

1. AGENCY USE ONLY (Leave blank)	2. REPORT DATE 14 Dec 94	3. REPORT TYPE AND DATES COVERED Final : Oct 91 - Oct 94

4. TITLE AND SUBTITLE Hypersonic Flow Research On Unstructured Grids Final Report	5. FUNDING NUMBERS AFOSR F49620-92-J-0085

6. AUTHOR(S)
Robert W. Walters, Principal Investigator,
Michael Applebaum, Graduate Assistant

7. PERFORMING ORGANIZATION NAME(S) AND ADDRESS(ES) Virginia Polytechnic Institute and State University Department Of Aerospace and Ocean Engineering Blacksburg, VA 24061	8. PERFORMING ORGANIZATION REPORT NUMBER AFOSR-TR. 9 5 - 0 3 0 2

9. SPONSORING/MONITORING AGENCY NAME(S) AND ADDRESS(ES) Air Force Office of Scientific Research Bolling Air Force Base Washington DC, 20332-6448	10. SPONSORING/MONITORING AGENCY REPORT NUMBER

NA

DTIC SELECTED JUN 1 1995 B

11. SUPPLEMENTARY NOTES

12a. DISTRIBUTION/AVAILABILITY STATEMENT APPROVED FOR PUBLIC RELEASE: DISTRIBUTION UNLIMITED	12b. DISTRIBUTION CODE

19950616 059

13. ABSTRACT (Maximum 200 words)

The main accomplishments under this effort include development of numerical algorithms for solving the Navier Stokes equations with higher order spatial discretizations, a generalized thermo-chemical model, and a one equation turbulence model on unstructured meshes. This report focuses attention on the implementation of the thermo-chemical modeling, viscous fluxes, turbulence modeling, and higher order spatial discretizations. Solutions are presented for an equilibrium air nozzle, RAM II-C reentry probe, Aeroassist Flight Experiment, an analytic forebody, and the turbulent flow over a flat plate.

DTIC QUALITY INSPECTED 5

14. SUBJECT TERMS Unstructured Flow Solver, Turbulence Modeling, Thermo-chemical Modeling, Higher Order Reconstruction	15. NUMBER OF PAGES 44
	16. PRICE CODE

17. SECURITY CLASSIFICATION OF REPORT Unclassified	18. SECURITY CLASSIFICATION OF THIS PAGE	19. SECURITY CLASSIFICATION OF ABSTRACT	20. LIMITATION OF ABSTRACT UL

Introduction

Over the years, computational fluid dynamics (CFD) has steadily gained acceptance as a beneficial tool for reducing the cost of designing aerospace vehicles. As the acceptance of CFD grows, many new applications are conceived which require new and more sophisticated algorithms to model the various physical processes associated with advanced vehicle design. One area of increasing interest is the design of hypersonic vehicles, such as the National Aerospace Plane (NASP), for which ground based wind tunnel testing is either technically or fiscally impractical.

During the past two decades, powerful numerical methods for solving the Navier-Stokes equations with real gas effects on structured meshes have been developed [1-2]. However, during the same time period, little in the way of progress has been accomplished in the area of efficiently solving the Navier-Stokes equations with real gas effects on unstructured meshes, in either two dimensions or three dimensions. Most of the recent successes in unstructured technology have been in the area of solving three dimensional inviscid perfect gas flows or two dimensional perfect gas viscous flows. While technically and theoretically simple, the implementation of the viscous fluxes along with finite rate chemistry models in practice becomes complicated by the nature of unstructured flow solvers.

For the work presented in this paper, a finite-volume technique has been chosen in keeping with a growing trend in the CFD community. Since the finite volume approach is derived from the integral conservation equations, it has the ability to properly capture flow discontinuities. The structure of this particular code allows the computational domain to be discretized into either triangles, quadrilaterals, or a combination of both in two dimensions, and tetrahedra, hexahedra, prisms, or any combination of these elements in three dimensions.

The emphasis of the current work centers on solution algorithm development. While grid generation is currently one of the limiting factors in the acceptance of unstructured flow solvers in CFD, suitable techniques are becoming more readily available.

Mathematical & Numerical Formulation

We begin the development of our numerical algorithm with the integral form of the three dimensional Navier Stokes equations,

$$\frac{\partial}{\partial t} \iiint_V Q \, dV + \oint_S \vec{F} \cdot \hat{n} \, ds - \oint_S \vec{G} \cdot \hat{n} \, ds = \iiint_V W \, dV \tag{1}$$

where Q represents the vector of dependent variables, W is the source term due to chemical reactions and non-equilibrium thermodynamics, $\vec{F} \cdot n$ and $\vec{G} \cdot n$ represent the inviscid and viscous flux of mass, momentum, and energy out of the control volume V through the surface S with $\hat{n}$ outward unit normal from S. In order to include real gas effects, the standard system of five equations has been augmented to include the effects of a generalized thermo-chemical model due to Grossman et. al. [3]. For our purposes, the effect is to replace the global continuity equations by N species continuity equations, where N is the number of species in the chosen chemistry model. In addition, to account for M species considered to be in thermal non-equilibrium, the system has been augmented to include

1

M non-equilibrium energy conservation equations. In light of this, the vector of dependent variables and thermo-chemical source terms are given by:

$$
Q = \begin{pmatrix} \rho_1 \\ \rho_2 \\ \vdots \\ \rho_N \\ \rho u \\ \rho v \\ \rho w \\ \rho_1 e_{n_1} \\ \rho_2 e_{n_2} \\ \vdots \\ \rho_N e_{n_M} \\ \rho e_o \end{pmatrix}, \qquad
W = \begin{pmatrix} \omega_1 \\ \omega_2 \\ \vdots \\ \omega_N \\ 0 \\ 0 \\ 0 \\ \dot{Q}_1 \\ \dot{Q}_2 \\ \vdots \\ \dot{Q}_M \\ 0 \end{pmatrix}
\tag{2}
$$

where ρ_i is the ith species density, ρ is the mixture density, u, v, and w are the components of the velocity vector in the principal directions $\hat{i}$, $\hat{j}$, and $\hat{k}$ respectively, e_{n_i} represents the ith species non-equilibrium energy contribution, e_o is the total energy, ω_i represents the source terms due to chemical reactions, and Q_i represents the source terms due to vibrational non-equilibrium thermodynamics. In equation (1) we assume body forces are negligible. The governing equations are closed by an equation of state relating the species densities, pressure and energy.

The inviscid flux vector $\vec{F}$ consists of components from the three principal directions,

$$
\vec{F} = f\hat{i} + g\hat{j} + h\hat{k}
\tag{3}
$$

where the flux components f, g, and h are given by:

$$
f = \begin{pmatrix} \rho_1 u \\ \rho_2 u \\ \vdots \\ \rho_N u \\ \rho u^2 + p \\ \rho u v \\ \rho u w \\ \rho_1 e_{n_1} u \\ \rho_2 e_{n_2} u \\ \vdots \\ \rho_M e_{n_M} u \\ \rho h_0 u \end{pmatrix}, \quad
g = \begin{pmatrix} \rho_1 v \\ \rho_2 v \\ \vdots \\ \rho_N v \\ \rho u v \\ \rho v^2 + p \\ \rho v w \\ \rho_1 e_{n_1} v \\ \rho_2 e_{n_2} v \\ \vdots \\ \rho_M e_{n_M} v \\ \rho h_0 v \end{pmatrix}, \quad
h = \begin{pmatrix} \rho_1 w \\ \rho_2 w \\ \vdots \\ \rho_N w \\ \rho u w \\ \rho v w \\ \rho w^2 + p \\ \rho_1 e_{n_1} w \\ \rho_2 e_{n_2} w \\ \vdots \\ \rho_M e_{n_M} w \\ \rho h_0 w \end{pmatrix}.
\tag{4}
$$

The discretization of the inviscid fluxes is accomplished by means of flux-vector and flux-difference splitting techniques. Flux-vector split techniques were originally developed for

perfect gas flows [4][5], and have been extended to flows in chemical equilibrium [6-9], and to flows in chemical and thermodynamic non-equilibrium [10-14]. Flux-vector split techniques have proven to be very accurate and robust when used for hypersonic flows [15] and are fully compatible with the conservative finite-volume approach.

Two of the more popular flux-vector split algorithms have been implemented into the unstructured flow solver. These are the algorithms developed by Steger and Warming [16] and Van Leer [17]. The basic idea of both methods is to split the inviscid flux vector in one dimension into two parts, one which contains the information that propagates downstream and one which contains the information that propagates upstream. The two parts are then constructed using extrapolation formulas consistent with the direction of propagation. Extension of the algorithms to more spatial dimensions is accomplished by superimposing pseudo-one dimensional problems.

In addition to the flux-vector splitting techniques, the flux difference splitting technique originally developed by Roe [18] has been implemented into the unstructured flow solver. While this method has proven to be less robust for hypersonic flows [15], it has been shown to be more accurate than the flux-vector split techniques. The flux difference splitting technique consist of an approximate Riemann solver, where an arbitrary discontinuity is supposed to exist between the left and right state. An approximate solution is written for this situation in terms of waves propagating upstream and downstream. In this case, the flux is not split, but reconstructed from the upstream and downstream contributions that constitute the left and right state of the Riemann problem.

Similar to the inviscid flux vector, the viscous flux vector $\vec{G}$ may be written in component form as:

$$\vec{G} = f_v \hat{i} + g_v \hat{j} + h_v \hat{k} \tag{5}$$

where the viscous flux components f_v, g_v, and h_v are given by:

$$f_v = \begin{pmatrix} 0 \\ 0 \\ \vdots \\ 0 \\ \tau_{xx} \\ \tau_{xy} \\ \tau_{xz} \\ 0 \\ 0 \\ \vdots \\ 0 \\ \bar{\tau}_x - q_x \end{pmatrix}, g_v = \begin{pmatrix} 0 \\ 0 \\ \vdots \\ 0 \\ \tau_{xy} \\ \tau_{yy} \\ \tau_{yz} \\ 0 \\ 0 \\ \vdots \\ 0 \\ \bar{\tau}_y - q_y \end{pmatrix}, h_v = \begin{pmatrix} 0 \\ 0 \\ \vdots \\ 0 \\ \tau_{xz} \\ \tau_{yz} \\ \tau_{zz} \\ 0 \\ 0 \\ \vdots \\ 0 \\ \bar{\tau}_z - q_z \end{pmatrix}. \tag{6}$$

In this formulation, mass diffusion has been neglected. The stresses in equation (6) are

3

written in terms of the velocity gradients via:

$$\tau_{xx} = \mu \left(2U_x - \frac{2}{3} \left(U_x + V_y + W_z \right) \right)$$

$$\tau_{yy} = \mu \left(2V_y - \frac{2}{3} \left(U_x + V_y + W_z \right) \right) \tag{6a}$$

$$\tau_{zz} = \mu \left(2W_z - \frac{2}{3} \left(U_x + V_y + W_z \right) \right)$$

$$\tau_{xy} = \mu \left(U_y + V_x \right)$$
$$\tau_{xz} = \mu \left(U_z + W_x \right) \tag{6b}$$
$$\tau_{yz} = \mu \left(V_z + W_y \right)$$

$$\bar{\tau}_x = U\tau_{xx} + V\tau_{xy} + W\tau_{xz}$$
$$\bar{\tau}_y = U\tau_{xy} + V\tau_{yy} + W\tau_{yz} \tag{6c}$$
$$\bar{\tau}_z = U\tau_{xz} + V\tau_{yz} + W\tau_{zz}$$

The heat flux terms in equation (6) are written in terms of the temperature gradients via:

$$q_x = -kT_x$$
$$q_y = -kT_y \tag{6d}$$
$$q_z = -kT_z$$

where μ is the laminar viscosity, k is the thermal conductivity, and T is the translational temperature. The subscript x, y, and z represent the gradient of the term in the corresponding spatial direction. The bulk viscosity, $\lambda = -2\mu/3$ is based on Stokes hypothesis, which is valid when Newtonian fluids are considered and bulk viscosity effects are neglected. Bulk viscosity effects should be accounted for when rotational non-equilibrium is present [19]. In addition bulk viscosity effects exhibit a significant influence on sound propagation and shock-wave structure [19].

Spatial Discretization

Since the finite-volume method is simply a discrete representation of the integral conservation laws, it has the property of properly capturing all flow discontinuities. In the finite-volume formulation, the domain is subdivided into a discrete number of control volumes. The variation of the flow quantities may then be approximated by a polynomial over each control volume. In this work we use a polynomial that satisfies several reconstruction criteria including *k-exactness*. The discrete equations are then solved simultaneously over each individual control volume. The particular functions describing the flow quantities within each control volume are used to evaluate the volume and surface integrals of the governing equations. The choice of these functions determine the spatial accuracy of the solution.

In discretizing the governing equations, the conserved variables Q must be integrated over each control volume, the fluxes must be integrated over all of the faces surrounding

4

each control volume, and the source terms W must be integrated over each control volume. The inviscid fluxes are discretized using a characteristic based flux-split algorithm, either Steger-Warming, Van Leer, or Roe's numerical flux function. All of these algorithms require that the dependent variables be interpolated from either side of each cell face. Therefore, procedures need to be developed which model the point-wise spatial variation of conservative variables Q in terms of the known cell averaged conservative variables $\bar{Q}$. The key to the success of any finite volume flow solver is the ability to accurately produce these point-wise variations in the flow variables.

Reconstruction

The problem of determining the point-wise variation of the flow variables from the cell averages is known as the reconstruction problem. Simply stated, the reconstruction problem involves the process of determining the point-wise distribution given the cell averages with the restriction that integrating the point-wise function recovers the cell averages. Mathematically this restriction becomes one of ensuring conservation of the mean

$$\bar{Q} = \frac{1}{V} \iiint_V Q(x, y, z) \, dV \tag{7}$$

For steady state solutions, the accuracy of the scheme is determined by the accuracy of the expressions used to evaluate the fluxes at the cell interface.

In the unstructured flow solver, three higher order reconstruction methods are employed. The first two are gradient based schemes proposed by Barth[20] and Frink[21]. For the problems presented here, those methods were passed up in favor of a k-exact formulation originally proposed by Barth[22]. The flavor of the k-exact formulation implemented in the unstructured code was developed by Mitchell and Walters [23]. For this method, the functional form for $Q(x, y, z)$ is a polynomial expression of degree 1 for second order accuracy.

$$Q(x, y, z) = C_0 + C_1 x + C_2 y + C_3 z \tag{8}$$

The use of the polynomial expression in equation (8) has three advantages which make it a desirable choice for implementation. First, the expressions are easily integrated over a control volume via simple quadrature formulas. Second, the computation of weak solutions is permissible via two independent states, Q_L and Q_R, which are evaluated at the cell interface. Discontinuities may then be resolved using an appropriate Riemann solver. Last and perhaps most important for our discussion, they are easily differentiated with respect to the spatial coordinates x, y, and z. This allows the computation of the gradients in the viscous fluxes to be performed with little additional computational effort.

In equation (8), there are four coefficients for each polynomial which must be solved for (in two dimensions the number of coefficients is reduced to three). Therefore, we need four cells in which we can apply the restriction, equation (7), to arrive at a linear system for the coefficients. For the second order accurate, $k = 1$ reconstruction considered here,

the four restrictions on our reconstruction polynomial becomes:

$$\frac{1}{V_1} \iiint_{V_1} Q(x,y,z) \ dx \ dy \ dz = \bar{Q}_1$$

$$\frac{1}{V_2} \iiint_{V_2} Q(x,y,z) \ dx \ dy \ dz = \bar{Q}_2$$

$$\frac{1}{V_3} \iiint_{V_3} Q(x,y,z) \ dx \ dy \ dz = \bar{Q}_3 \qquad (9)$$

$$\frac{1}{V_4} \iiint_{V_4} Q(x,y,z) \ dx \ dy \ dz = \bar{Q}_4$$

where the subscript 1 denotes the first cell in the stencil, 2 the second cell in the stencil, and so on. In equation (9), the polynomial function for $Q(x,y,z)$ is the same for each of the equations. For our purposes, any acceptable second order quadrature rule is satisfactory,

$$\frac{1}{V} \iiint_V Q(x,y,z) = Q(\bar{x},\bar{y},\bar{z}) + O(h^2) \qquad (10)$$

where $\bar{x}$, $\bar{y}$, and $\bar{z}$ specify the location of the cell centers. Therefore, when the quadrature rule is applied to equation (9) we arrive at a linear system for the reconstruction polynomials.

$$\begin{bmatrix} 1 & \bar{x}_1 & \bar{y}_1 & \bar{z}_1 \\ 1 & \bar{x}_2 & \bar{y}_2 & \bar{z}_2 \\ 1 & \bar{x}_3 & \bar{y}_3 & \bar{z}_3 \\ 1 & \bar{x}_4 & \bar{y}_4 & \bar{z}_4 \end{bmatrix} \begin{pmatrix} C_0 \\ C_1 \\ C_2 \\ C_3 \end{pmatrix} = \begin{pmatrix} \bar{Q}_1 \\ \bar{Q}_2 \\ \bar{Q}_3 \\ \bar{Q}_4 \end{pmatrix} \qquad (11)$$

Equation (11) can be solved directly via symbolic inversion. Substitution into equation (8) yields an expression for $Q(x,y,z)$ in terms of the centroids of the stencil cells and the cell average variables. For a stencil which is fixed in time, the only part of the expression which changes are the values of the cell averaged variables. Therefore, we may rewrite equation (8) as a vector of reconstruction weights $\vec{\omega}$ and a vector of the cell averaged variables $\bar{Q}$:

$$Q(x,y,z) = \begin{pmatrix} \omega_1(x,y,z) \\ \omega_2(x,y,z) \\ \omega_3(x,y,z) \\ \omega_4(x,y,z) \end{pmatrix} \begin{pmatrix} \bar{Q}_1 & \bar{Q}_2 & \bar{Q}_3 & \bar{Q}_4 \end{pmatrix} \qquad (12)$$

where the spatial dependency come in the form of the reconstruction weights. With a simple second order accurate flux integration, the weights may be determined once at the beginning of a solution thereby reducing the computational effort and storage requirements.

Discretization of the Viscous Fluxes

The discretization of the viscous fluxes is dependent upon the method of reconstruction used to determine the point-wise variation of the conservative variables from the

cell averaged values. The discussion in this section is based on the k-exact reconstruction method, however, the methods developed are general enough that extension to other reconstruction methods is straightforward.

For the k-exact reconstruction method, the gradients may be determined by simple differentiation of the reconstruction polynomials with respect to the spatial coordinates. In terms of the weights, the gradients of the u velocity component become:

$$
\begin{aligned}
U_x &= \omega_{1_x}\bar{U}_1 + \omega_{2_x}\bar{U}_2 + \omega_{3_x}\bar{U}_3 + \omega_{4_x}\bar{U}_4 \\
U_y &= \omega_{1_y}\bar{U}_1 + \omega_{2_y}\bar{U}_2 + \omega_{3_y}\bar{U}_3 + \omega_{4_y}\bar{U}_4 \\
U_z &= \omega_{1_z}\bar{U}_1 + \omega_{2_z}\bar{U}_2 + \omega_{3_z}\bar{U}_3 + \omega_{4_z}\bar{U}_4
\end{aligned}
\tag{13}
$$

where ω_{1_x} is the partial derivative of the reconstruction weight with respect to the x spatial coordinate. The other gradients in equations 6(a)-6(d) are determined in a similar fashion.

The transport properties are computed from the reconstructed values at the interface. In other words, for Sutherland's law, the temperature at the cell interace is first computed, from which the viscosity and thermal conductivity may then be computed. This eliminates the need to reconstruct the transport properties themselves. The computation of the species and mixture transport properties are discussed shortly.

Once the gradients are computed the viscous fluxes may be computed via:

$$
\vec{G} = \begin{pmatrix}
0 \\
0 \\
\vdots \\
0 \\
\eta_x \tau_{xx} + \eta_y \tau_{xy} + \eta_z \tau_{xz} \\
\eta_x \tau_{xy} + \eta_y \tau_{yy} + \eta_z \tau_{yz} \\
\eta_x \tau_{xz} + \eta_y \tau_{yz} + \eta_z \tau_{zz} \\
0 \\
0 \\
\vdots \\
0 \\
\eta_x \left(\bar{\tau}_x - q_x \right) + \eta_y \left(\bar{\tau}_y - q_y \right) + \eta_z \left(\bar{\tau}_z - q_z \right)
\end{pmatrix}
\tag{14}
$$

where η is the outward normal and η_x is the x-component of the outward normal.

Viscosity Coefficient

The laminar viscosity coefficient (μ) is computed for each species in the chemistry model using curve fits which are based on experimental data. The advantage of using curve fits is their simplicity and availability of semi-empirical rules for recovering the mixture values. Two experimental curve fits are available in the unstructured code. The first is one of the most widely adopted curve fits due to Blottner [24],

$$
\mu_s = exp[(A_s \ln T + B_s) \ln T + C_s] \quad s = 1, \ldots, N
\tag{15}
$$

7

where A_s, B_s, and C_s are coefficients determined from fitting the experimental data. Another popular experimental curve fit is due to Sutherland,

$$\mu_s = T^{1.5}\frac{E_s}{T + F_s}, \quad s = 1, \dots, N \tag{16}$$

where E_s and F_s are empirically derived.

The mixture viscosity coefficient is determined via Wilke's semi-empirical rule [25], which is based on kinetic theory,

$$\mu = \sum_{s=1}^{N} \frac{X_s \mu_s}{\sum_j^N X_j \phi_{sj}}, \tag{17}$$

where

$$\psi_{sj} = \frac{1}{\sqrt{8}}(1 + \frac{M_s}{M_j})^{-1/2}\left[1 + \sqrt{\frac{\mu_s}{\mu_j}}\left(\frac{M_j}{M_s}\right)^{1/4}\right]^2 \tag{18}$$

and X_s is the mole fraction of species s.

Thermal Conductivity Coefficient

Like the species viscosity, the species thermal conductivity is computed from experimental curve fits. One such curve fit is Eucken's relation,

$$k_s = \mu_s\left(\frac{3}{2}\tilde{c}_{v_{tr,s}} + \tilde{c}_{v_s}\right), \quad s = 1, ; N \tag{19}$$

where $\tilde{c}_{v_{tr,s}}$ is the translational contribution to the specific heat at constant volume. For a perfect gas, with $\tilde{\gamma} = 7/5$, Eucken's formula returns a Prandtl number $Pr = 0.737$, which is in good agreement with experimental values.

A second curve fit, due to Sutherland, has been implemented for determining the species thermal conductivity. The form of this curve fit is given by

$$k_s = T^{1.5}\frac{E_s}{T + F_s}, \quad s = 1, \dots, N \tag{20}$$

where the constants E_s and F_s are determined from experimental data.

The mixture thermal conductivity is computed using Wilke's mixture rule [25],

$$k = \sum_{s=1}^{N} \frac{X_s k_s}{\sum_j^N X_j \phi_{sj}}, \tag{21}$$

where the $\phi_{s,j}$ are the same as in the formulation for the mixture viscosity coefficient.

A simplified method for determining the mixture thermal conductivity has been implemented by assuming a constant Prandtl number and using the definition of the Prandtl number,

$$k = \frac{\mu \tilde{c}_p}{Pr}, \quad where\ Pr = constant \tag{22}$$

8

In this formulation, the species thermal conductivities are not required.

Stencil selection

One of the more challenging tasks associated with the k-exact formulation is the selection of the cells which complete each stencil. For the inviscid fluxes, two such stencils are required, one for the left state and one for the right state. For the viscous stencil, only one stencil is required, typically a centered stencil.

Figure 1(a) shows a two dimensional triangular mesh with a representative upwind stencil. In figure 1(a), the bold face represents the face for which the stencil must be generated. The circled numbers represent the cells which would complete the two dimensional stencil. In two dimensions three cells are required to complete the system of equations for a $k = 1$ reconstruction. In three dimensions four cells are required for a $k = 1$ reconstruction.

The inviscid stencil selection process begins by gathering the cells adjacent to the face, in this case, cell C_1 and C_2 which we refer to as the parent cell and biased cell respectively. The next step is to gather the cells surrounding the parent cell (C_{11} and C_{12}). For the case of a triangular mesh, the selection process would simply choose the parent cell and its two surrounding cells. The stencil would then be tested to ensure it was a valid stencil and if it failed either the biased cell would be used or the surrounding cells of C_{11} and C_{12} would be added to the possible list of cells. For quadrilateral meshes, where there are four cells from which to choose, the dot product of the cell centroid with the face metric is used as a basis for determining which cells to include in the stencil. In this case, the two surrounding cells with the smallest dot product and the parent cell is typically used. In three dimensions the process becomes complicated by the fact that four cells are required and poor stencils show up more readily than in two dimensions. In the unstructured code, several different methods for determining the inviscid and viscous stencil are provided. In three dimensions, it was found that a condition number test on the 4×4 coefficient matrix produced the best results to date. This requires an extra step in the stencil selection process. After gathering all of the cells which are to be considered for inclusion into the stencil, we need to construct a group of valid stencils for which we are going to apply the condition number test. Instead of testing every possible stencil which can be an enormous task, the algorithm can be simplified by restricting how we define our stencils. In our case, we consider only stencils made up of cells which share a face with at least one other cell in the stencil. We use the term continuous stencil to refer to these types of stencils. At this point it is too early to say whether a continuous stencil provides a more stable solution algorithm.
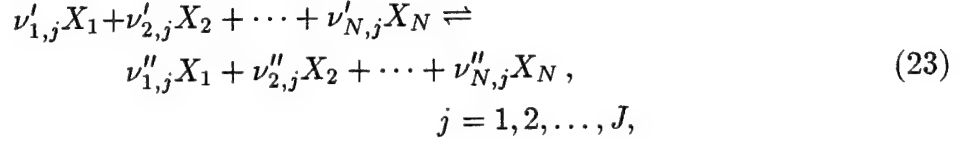
Figure 1(b) shows a two dimensional triangular mesh with a representative viscous stencil. In this figure, the bold face represents the face for which the flux is being computed. The circled numbers represent the cells which would be chosen to complete the stencil.

For the viscous stencil, a centered stencil is desirable. The selection process is similar to the inviscid stencil with the exception that the cells surrounding both the parent and biased cell are gathered. The stencil is then chosen from the parent, biased, and one of the surrounding cells. As with the inviscid stencil selection, test may be applied directly to the cells or to the stencils.

Chemical Source Terms

Following the work of Grossman and Cinnella [3], we have implemented thermo-chemical models into the flow solver. A brief description of the models is presented here for completeness. A fairly general simulation of chemical effects can be included in the governing equations, for a system containing N species in which J reactions take place

$$\nu'_{1,j}X_1 + \nu'_{2,j}X_2 + \cdots + \nu'_{N,j}X_N \rightleftharpoons$$
$$\nu''_{1,j}X_1 + \nu''_{2,j}X_2 + \cdots + \nu''_{N,j}X_N, \tag{23}$$
$$j = 1, 2, \ldots, J,$$

The $\nu'_{i,j}$ and the $\nu''_{i,j}$ are the stoichiometric coefficients of the reactants and products of species X_i in the jth reaction, respectively. In the source vector W, the rate of production of species i may be written as [26]

$$\dot{w}_i \equiv \frac{d\rho_i}{dt} = \mathcal{M}_i \sum_{j=1}^{J} (\nu''_{i,j} - \nu'_{i,j})$$
$$\left[k_{f,j} \prod_{l=1}^{N} \left(\frac{\rho_l}{\mathcal{M}_l} \right)^{\nu'_{i,j}} - k_{b,j} \prod_{l=1}^{N} \left(\frac{\rho_l}{\mathcal{M}_l} \right)^{\nu''_{i,j}} \right], \tag{24}$$
$$i = 1, 2, \ldots, N$$

where for reaction j the forward and backward reaction rates, $k_{f,j}$ and $k_{b,j}$, are assumed to be known functions of temperature, and are related by thermodynamics

$$k_{b,j} = \frac{k_{f,j}}{K_{e,j}} \tag{25}$$

The equilibrium constant, $K_{e,j}$, is a known function of the thermodynamic state. Using this relation, we obtain

$$\dot{w}_i \equiv \frac{d\rho_i}{dt} = \mathcal{M}_i \sum_{j=1}^{J} (\nu''_{i,j} - \nu'_{i,j}) k_{f,j}$$
$$\left[\prod_{l=1}^{N} \left(\frac{\rho_l}{\mathcal{M}_l} \right)^{\nu'_{i,j}} - \frac{1}{K_{e,j}} \prod_{l=1}^{N} \left(\frac{\rho_l}{\mathcal{M}_l} \right)^{\nu''_{i,j}} \right], \tag{26}$$
$$i = 1, 2, \ldots, N$$

Note, the term in the brackets goes to zero when equilibrium compositions are reached for ρ_i, since it reduces to a formulation of the Law of Mass Action

$$K_{e,j} = \frac{\prod_{l=1}^{N} (\rho_l/\mathcal{M}_l)^{\nu''_{i,j}}}{\prod_{l=1}^{N} (\rho_l/\mathcal{M}_l)^{\nu'_{i,j}}}, \qquad j = 1, \ldots, J \tag{27}$$

valid for equilibrium concentrations.

The unstructured flow solver currently contains 28 chemistry models, of which 5 are air chemistry and 18 are hydrogen-air chemistry. In addition, there are approximately 450 reactions and 34 species from which to choose.

Internal Energy

Assuming each species in the gas mixture behaves as a thermally perfect gas, the internal energy, e_i may be defined as

$$e_i = \tilde{e}_i(T) + e_{n_i} \tag{28}$$

where $\tilde{e}_i$ is the known equilibrium portion of the energy, T is the translational temperature, and e_{n_i} is the non-equilibrium portion of the energy. The portion of the internal energy due to electronic excitation has been neglected [19].

It is convenient to express the equilibrium portion of the internal energy, $\tilde{e}_i$, in terms of a specific heat at constant volume, $\tilde{c}_{v_i}$, as follows

$$\tilde{e}_i = \int_{T_{ref}}^{T} \tilde{c}_{v_i}(\tau) \, d\tau + h_{f_i} \tag{29}$$

where $\tilde{c}_{v_i} = d\tilde{e}_i/dT$, and h_{f_i} is the heat of formation of species i.

The internal energy of a gas mixture composed of N species, with the first M species assumed to contain a non-equilibrium portion of their internal energy may be written as

$$e = \sum_{i=1}^{N} \frac{\rho_i}{\rho} e_i = \sum_{i=1}^{N} \frac{\rho_i}{\rho} \tilde{e}_i + \sum_{i=1}^{M} \frac{\rho_i}{\rho} e_{n_i} \tag{30}$$

The mixture gas constant is given by

$$\tilde{R} \equiv \sum_{i=1}^{N} \frac{\rho_i}{\rho} R_i \tag{31}$$

Equation of State

A very important assumption that has been made is the consideration of *weakly interacting* particles, where the interaction potential is decaying very rapidly in space and is negligible after a typical distance of the order of the particle radius. The most noticeable effect of this assumption is that the mixture components will behave as *thermally perfect* gases, where the internal energy is only a function of temperature. Strictly related to this result is the validity of Dalton's Law, whereby the mixture pressure is the summation of partial pressures. The applicability of the weak-interaction assumption is restricted to conditions of low density and moderate to high temperature. Many flows of engineering interest meet these requirements.

Consequently, the relationship between pressure and temperature will read

$$p = \sum_{i=1}^{N} \rho_i R_i T = \rho \tilde{R} T \tag{32}$$

where the mixture density is given by

$$\rho = \sum_{i=1}^{N} \rho_i \tag{33}$$

and where the mixture gas constant, $\tilde{R}$, is defined by (31). In equation (32), we have made the simplifying assumption that the translational temperature is the same for each species, $T_i = T$. This simplification is reasonable for flows where the mass of the molecules in the mixture are on the same order of magnitude. Thus, this will not hold for flows with free electrons.

The state relationship of the pressure to the specific internal energy occurs implicitly through the temperature. For a given chemical composition, internal energy and non-equilibrium energy, the temperature must be evaluated from

$$e = \sum_{i=1}^{N} \frac{\rho_i}{\rho} \tilde{e}_i(T) + \sum_{i=1}^{M} \frac{\rho_i}{\rho} e_{n_i}. \tag{34}$$

Iterative procedures could then be used to solve for T. Once T is found, the pressure may be evaluated from (32). However, our unstructured code integrates the primitive variables ρ_i, u, v, w, e_{n_i}, and p in time. Therefore, this additional iterative procedure is not required since the temperature T can be found directly from the pressure p. The implementation of time integration schemes applied to the primitive variables while retaining the conservative property is straightforward.

Non-Equilibrium Thermodynamics

The nonequilibrium thermodynamic model groups the translational and rotational contributions in $\tilde{e}_i$, thus considering them in equilibrium at the translational temperature T.

$$\tilde{e}_i = n_i R_i T + h_{f_i}, \qquad i = 1, \dots, N \tag{35}$$

In this equation, the constants n_i are given by

$$n_i = \begin{cases} \frac{3}{2} & \text{for monotomic species,} \\ \frac{5}{2} & \text{for diatomic \& linear polyatomic species,} \\ \frac{7}{2} & \text{for nonlinear polyatomic species.} \end{cases}$$

Vibrational contributions are assumed to be in non-equilibrium and electron excitation has been neglected. As a result, this model should be restricted to use with air chemistry models.

The elastic contribution to the source terms in the non-equilibrium vibrational energy equation can be modeled by considering the exchanges between the vibrational and translational-rotational contributions to the internal energy. The rate of energy exchange between the vibrational and translational-rotational modes are assumed to be of a Landau-Teller form,

$$\left(\dot{Q}_s\right)_{n,E} = \rho_s \frac{e_{v_s}^*(T) - e_{n_s}}{\tau_s} \qquad s = 1, \ldots, M, \tag{36}$$

where e_v^* is the equilibrium vibrational contribution to the internal energy at the translational temperature T

$$e_{v_s}^* = \frac{R_s \theta_{v_s}}{e^{\theta_{v_s}T} - 1}, \tag{37}$$

and τ is a relaxation time given by Millikan and White [27]

$$\tau_s = \frac{1.013 \ 10^5}{p} \exp\left[A_{ss}(T^{-1/3} - 0.015\mu_{ss}^{1/4}) - 18.42\right], \tag{38}$$

where

$$A_{ss} = 1.16 \ 10^{-3} \mu_{ss}^{1/2} \theta_{v_s}^{4/3}, \qquad \mu_{ss} = \frac{\mathcal{M}_s \mathcal{M}_s}{\mathcal{M}_s + \mathcal{M}_s} \tag{39}$$

The inelastic contribution can be modeled by taking into account chemical reactions

$$\left(\dot{Q}_s\right)_{n_I} = \dot{\omega}_s e_{n_s} \tag{40}$$

where no attempt has been made to consider coupling effects though equivalent temperatures or by other means. The total source term for the non-equilibrium energy equation is given by the sum of the elastic and inelastic contributions,

$$\left(\dot{Q}_s\right)_n = \left(\dot{Q}_s\right)_{n,E} + \left(\dot{Q}_s\right)_{n,I} \tag{41}$$

Equilibrium Thermodynamics

Two thermal equilibrium models are implemented in the unstructured code. The first model is a thermal equilibrium model where $e_{n_i} \equiv 0$ and vibrational contributions are included into $\tilde{e}_i$ by means of a simple harmonic oscillator formula

$$\tilde{e}_i = n_i R_i T + \frac{R_i \Theta_{v,i}}{e^{\Theta_{v,i}/T} - 1} + h_{f_i}, \quad i = 1, \ldots, N \tag{42}$$

where $\Theta_{v,i}$ are characteristic vibrational temperatures. More than one characteristic temperature will appear in the formulas for polyatomic molecules. In this model we have neglected electronic excitation. Therefore, this model is applicable to air chemistry models.

13

The second model is a thermal equilibrium model where polynomials are used to curve fit $\tilde{c}_{v_i}$ [28]

$$\tilde{c}_{v_i} = a_1/T^2 + a_2/T + a_3 + a_4 T + a_5 T^2 \\ + a_6 T^3 + a_7 T^4 + a_8 T^5 \tag{43}$$

from which the internal energy can be found from

$$\tilde{e}_i = \int_{T_{ref}}^{T} \tilde{c}_{v_i}(\tau)\, d\tau + h_{f_i} \tag{44}$$

For the 34 species currently implemented in our database, the valid temperature range for the curve fits is from 200 K to 6,000 K.

Turbulence Modeling

With the growing acceptance and use of computational fluid dynamics, many new applications are conceived which require new and more sophisticated algorithms to model the various physical processes associated with current vehicle design. Since most of the flows of interest in practice are turbulent, one component required to successfully model these complex flows is the modeling of turbulence. In this work, we have implemented the Spalart and Allmaras one equation turbulence model [29].

One equation models use one additional field equation to specify a velocity scale. Historically the velocity scale chosen for one-equation models is the turbulent kinetic energy (TKE). However, one equation models based on the turbulent kinetic energy still require an algebraic relation for the length scale which leads to results not very different from the algebraic models. Like the algebraic models, these models are cumbersome to implement in an unstructured format. A new group of one equation models has been developed in which the field equation represents a transport equation for the turbulence viscosity. These new one equation models are "local" in that the equation at one point does not depend on the solution at other points and therefore are compatible with both structured and unstructured grid topologies.

Transport Equation

A summary of the original model as presented in the original Spalart and Allmaras paper [29] is briefly reviewed here. The differential transport equation along with all relevant closure coefficients and auxiliary relations are provided. Immediately following the discussion on the differential form of the governing equation is the integral form of the transport equation suitable for a finite volume fluid dynamics code.

Differential Formulation

Our discussion closely follows the appendix of the Spalart and Allmaras paper with two exceptions. The implementation followed here does not include the optional trip function required for transition. Due to the removal of this term, the boundary and initial conditions must also be slightly modified from those discussed in the appendix of the original paper.

The one-equation model provides a single differential transport equation for the turbulent quantity, $\tilde{\nu}$. The dependent variable in the transport equation is related to the eddy viscosity ν_t by:

$$\nu_t = \tilde{\nu} f_{v1}, \qquad f_{v1} = \frac{\chi^3}{\chi^3 + C_{v1}^3}, \qquad \chi = \frac{\tilde{\nu}}{\nu} \tag{45}$$

where $\tilde{\nu}$ is the dependent (working) variable and ν is the molecular viscosity (μ/ρ). The differential form of the transport equation for the dependent variable is given by:

$$\frac{D\tilde{\nu}}{Dt} = C_{b1}\tilde{S}\tilde{\nu} - C_{w1}f_w \left[\frac{\tilde{\nu}}{d}\right]^2 +$$
$$\frac{1}{\sigma}\left[\nabla \cdot \left((\nu + \tilde{\nu})\nabla\tilde{\nu}\right) + C_{b2}\left(\nabla\tilde{\nu}\right)^2\right], \tag{46}$$

The difference between equation (46) and equation (A2) in [29] is the absence of the tripping functions required for modeling transition. This is equivalent to setting the closure coefficients C_{t1} and C_{t3} to zero in the equations provided in the appendix of [29]

The transport equation (46) represents on the left side a local time rate of change and convective acceleration via the material derivative, and on the right hand side from left to right a production term, destruction term, and two diffusion terms, respectively.

The auxiliary relations required to complete the production term are given by:

$$\tilde{S} = S + \frac{\tilde{n}u}{\kappa^2 d^2}f_{v2} \qquad f_{v2} = 1 - \frac{\chi}{1 + \chi f_{v1}} \tag{47}$$

where S is the magnitude of the vorticity and given in terms of the velocity gradients using tensor notation

$$S = \sqrt{2\Omega_{ij}\Omega_{ij}}, \qquad \Omega_{ij} = \frac{1}{2}\left(\frac{\partial U_i}{\partial X_j} - \frac{\partial U_j}{\partial X_i}\right) \tag{48}$$

and d is the distance to the nearest solid boundary.

The auxiliary relations required to complete the destruction term are provided by:

$$f_w = g\left[\frac{1 + c_{w3}^6}{g^6 + c_{w3}^6}\right]^{1/6}, \qquad g = r + c_{w2}\left(r^6 - r\right),$$
$$r = \frac{\tilde{n}u}{\tilde{S}\kappa^2 d^2} \tag{49}$$

For large values of r, the function f_w reaches a constant. Therefore, values of r greater than 10 may be truncated.

The model is completed by the closure coefficients. The coefficients are $c_b1 = 0.1355$, $c_b2 = 0.622$, $\kappa = 0.41$, $\sigma = 2/3$, $c_w1 = c_b1/\kappa^2 + (1 + c_b2)/\sigma$, $c_w2 = 0.3$, $c_w3 = 2$, and $c_{v1} = 7.1$.

Turbulent heat transfer is computed using a constant turbulent Prandtl number input by the user (typically equal to 0.9). The turbulent thermal conductivity is then computed using the definition of the Prandtl number

$$k_t = \frac{\mu_t C_p}{\sigma_t} \tag{50}$$

where k_t is the turbulent thermal conductivity, $\mu_t = \rho \nu_t$ is the turbulent viscosity, C_p is the mixture specific heat, and σ_t is the turbulent Prandtl number.

The boundary conditions for the turbulence viscosity are simple and easily implemented. For wall bounded flows, the wall boundary condition is to set the turbulence viscosity to zero ($\tilde{\nu} = 0$). All other boundary conditions are fixed at the freestream. The initial condition is set to the freestream turbulence viscosity. The freestream turbulence viscosity is input by the user, however, a value roughly equal to 10 times the molecular viscosity has been found to produce adequate results. It should be noted that this is different from the values proposed in the original model. The values provided in the original model assume the triping term is implemented.

The integral conservation form of the turbulence model transport equation may be written as:

$$\frac{\partial}{\partial t} \iiint_V \tilde{\nu} \, dV + \iint_S \tilde{\nu} \left(\vec{V} \cdot \hat{n} \right) dS - \iiint_V \tilde{\nu} \, \nabla \cdot \vec{V} \, dV =$$

$$\iiint_V \left(C_{b1} \tilde{S} \tilde{\nu} - C_{w1} f_w \left[\frac{\tilde{\nu}}{d} \right]^2 + \frac{C_{b2}}{\sigma} \left(\nabla \tilde{\nu} \cdot \nabla \tilde{\nu} \right) \right) dV + \tag{51}$$

$$\iint_S \left(\frac{1}{\sigma} \left(\nu + \tilde{\nu} \right) \nabla \tilde{\nu} \cdot \hat{n} \right) dS$$

The auxiliary functions and closure coefficients remain the same for the integral transport equation.

Convective Flux

The convective flux,

$$\iint_S \tilde{\nu} \left(\vec{V} \cdot \hat{n} \right) dS \tag{52}$$

has been implemented into the unstructured flow solver with two different methods. In both methods, regions where the Mach number is greater than unity, a full upwind biased flux is used. In regions where the Mach number is less than unity, either a full flux is used or a flux vector splitting is used depending on user preference. At this point it is too early to determine whether one method has a distinct advantage over the other.

The left and right state vectors (solution and thermodynamic property arrays) are determined using a first order reconstruction. If we denote the $x,y,$ and z metrics by η_x, η_y, and η_z respectively, we compute the left and right Mach numbers via:

$$\begin{aligned} \bar{U}_l &= \eta_x u_l + \eta_y v_l + \eta_z w_l & M_l &= \bar{U}_l / a_l \\ \bar{U}_r &= \eta_x u_r + \eta_y v_r + \eta_z w_r & M_r &= \bar{U}_r / a_r \end{aligned} \tag{53}$$

where u, v, and w are the x, y, and z components of velocity, M is the Mach number, and a the speed of sound. Based on the magnitude and sign of the Mach numbers, the method of computing the convective flux is determined.

If the left state Mach number is greater than unity ($M_l > 1$) then the flux is computed using a full upwind biased stencil,

$$F = \bar{U}_l \tilde{\nu}_l \tag{54}$$

16

and in a similar fashion, if the right state Mach number is less than -1 then the flux is computed using ,

$$F = \bar{U}_r \tilde{\nu}_r \tag{55}$$

Obviously, in both cases the flow is supersonic and an upwind stencil is desirable.

Regions where the flow is subsonic, the convective flux is computed using either a full flux,

$$F = \frac{1}{2} \left(\bar{U}_l \tilde{\nu}_l + \bar{U}_r \tilde{\nu}_r \right) \tag{56}$$

or a split flux which follows the Van Leer flux vector splitting scheme discussed in the earlier sections,

$$F = \left(\frac{1}{4} \left(M_l + 1 \right)^2 a_l \right) \tilde{\nu}_l - \left(\frac{1}{4} \left(M_r - 1 \right)^2 a_r \right) \tilde{\nu}_r \tag{57}$$

Diffusive Flux

The diffusive flux,

$$\iint_S \left(\frac{1}{\sigma} \left(\nu + \tilde{\nu} \right) \nabla \tilde{\nu} \cdot \hat{n} \right) \, dS \tag{58}$$

is computed in a similar fashion to the viscous fluxes. The same reconstruction weights that were used to compute the viscous fluxes are used to compute the turbulence model diffusive flux. Recall, that in general there are four reconstruction weights for $k = 1$ reconstruction in three dimensions. The variables are reconstructed to the face via the reconstruction weights,

$$\tilde{\nu}_{face} = \omega_1 \tilde{\nu}_1 + \omega_2 \tilde{\nu}_2 + \omega_3 \tilde{\nu}_3 + \omega_4 \tilde{\nu}_4 \tag{59}$$

where ω_i is the reconstruction weight for the ith cell in the reconstruction stencil and $\tilde{\nu}_i$ is the cell centered value of the reconstructed variable. The molecular viscosity is reconstructed in the same manner.

The gradients are computed using the partial derivatives of the reconstruction weights. Recall that for $k = 1$ and greater reconstructions, the weights are a function of spatial coordinates x, y, and z. Therefore, the gradients of the turbulence viscosity may be computed using

$$\frac{\partial \tilde{\nu}}{\partial x} = \omega_{1x} \tilde{\nu}_1 + \omega_{2x} \tilde{\nu}_2 + \omega_{3x} \tilde{\nu}_3 + \omega_{4x} \tilde{\nu}_4 \tag{60}$$

where ω_{ix} is the partial derivative of the ith reconstruction weight with respect to the x spatial coordinate. The gradients in the other spatial coordinate directions are obtained in the same manner. The formulation of the reconstruction weights and their derivatives for a $k = 1$ reconstruction are given in [30].

Distance Function

From an unstructured coding point of view, the computation of the distance function represents the greatest challenge in implementing the one equation turbulence model. The

17

distance function may be computed very accurately at the expense of CPU resources, or it may be approximated to a lower degree of accuracy with little CPU resources expended.

At this point, a simple, efficient approach for finding the distance from the cell center to the closest wall was chosen. The algorithm begins by gathering all of the faces on the boundary patches which compose our solid surface. From this list of boundary faces, a simple search is done finding the minimum distance from each face centroid to the given cell centroid. Once the closest face centroid is determined, the distance to the nodes of this face are computed and the minimum of the distances is taken to be our distance to the wall. Graphically, this is shown in figure 2.

In figure 2, the face centroids are shown as solid circles, the nodes of the closest face as empty circle, the further distances are represented as dashed lines, and the closest distance is represented by the solid line. In this case, the face centroid labeled as F_4 is the closest face, and the node labeled N_1 is the minimum distance from the cell centroid. Therefore, in this simple algorithm, this distance would be used as the distance from the cell centroid to the wall (d).

Time Integration

The time-dependent formulation of the governing equations has been chosen and is valid for time-dependent and steady state problems. The very small time scales associated with finite-rate chemistry can often make completely explicit time integration strategies for flows with strong chemical reactions impractical. Linearization of the chemical reaction source terms helps to eliminate the stability constraints associated with the chemical reactions and allows the use of practical time steps in performing both steady state and time dependent calculations. Once the linearizations of the various components of the governing equations have been obtained, they may be coupled with any of the current implicit time integration techniques for unstructured discretizations. Thus any advances in time integration techniques for perfect gas unstructured discretions may be quickly applied to the current algorithm.

One implicit time integration scheme which has received a lot of recent interest is the Generalized Minimum Residual (GMRES) algorithm originally proposed by Saad and Schultz[31]. The GMRES algorithm has been successfully adapted to both structured flow solvers[32] and unstructured flow solvers[33]. The GMRES implicit time integration technique is one of several chosen for implementation in the unstructured flow solver. The others include explicit m-stage Runge-Kutta with implicit residual smoothing and Jacobi iteration as an inner iterative technique for the Euler implicit method [30].

Results

Test cases were sought which would adequately test the individual components of the unstructured fluid dynamics code. Here we present several of these test cases.

The first of these solutions is chemically reacting air flowing through a supersonic nozzle. The air is assumed to be in chemical and thermodynamic equilibrium.

The second case corresponds to the chemically reacting flow field about the RamII-C reentry probe. For this problem the air is assumed to be in chemical and thermodynamic non-equilibrium.

The third solution presented is the aeroassist flight experiment (AFE) at Mach 10 and Mach 31.7. Solutions for the Mach 10 test case are compared to experimental data. The Mach 31.7 solutions are compared to other numerical studies of the AFE.

The fourth solution presented is an analytic forebody. The analytic forebody is a three dimensional, inviscid, supersonic flow over the cockpit of a high performance aircraft. The analytic forebody has been studied both numerically and experimentally [34] This problem was chosen to test the three dimensional k-exact reconstruction algorithm.

The last set of solutions presented are designed to test the viscous fluxes and the turbulence model. The first solution in this set is the subsonic, laminar flow over a two dimensional flat plate. The numerical solution is compared against the analytical solution of Blasius. The second solution is the supersonic, turbulent flow over the same flat plate. For this case, solutions are compared against the experimental data curve fit of Clauser [35].

Axi-symmetric Nozzle With Kang & Dunn Air Chemistry

The first solution presented is chemically reacting air flowing through a diverging supersonic nozzle. The cross section of the nozzle is circular with the cross sectional radius described by the function

$$ r = 0.125 \, L \left[1 + \sin(\pi X / 2L) \right], \qquad L = 2 \, m $$

where X is the streamwise location.

Using the Kang & Dunn air model [36], solutions were obtained for inflow conditions corresponding to air in thermodynamic and chemical equilibrium at a Mach number of 1.39 with a temperature of 9000 K and a mixture density of $3.856 \times 10^{-2} Kg/m^3$.

Solutions were obtained on three different grid types; a structured hexahedral grid, a fully unstructured hexahedral grid, and an unstructured prism grid. In addition, the solution was obtained on 5 different levels of grid refinement for each mesh type, with level 1 representing the coarsest mesh and level 5 representing the finest mesh. Previous solutions for the unstructured meshes were interpolated to the next mesh level using a simple quad tree algorithm.

Figures 3(a) through 3(d) show the level 1 through level 4 prism meshes. Figures 4(a) through 4(d) show the level 1 through level 4 hexahedral meshes. Provided with the figures is the number of cells, faces, and nodes for each mesh.

Figures 5(a) and 5(b) show the centerline N_2 mass fraction profiles for the level 4 and level 5 meshes. From these two figures, we see that grid refinement has little effect on the mass fraction profiles for this problem. In addition, the solutions on the different mesh types agree. Also evident from these figures is that assuming equilibrium mass fractions in the inflow has little effect on the mass fraction profiles.

Figures 6(a) and 6(b) show the temperature profile along the centerline. From these figures we see a large dependency between the different meshes. The prism solutions differ rather dramatically from the two hexahedral solutions towards the center of the nozzle. In addition, the solutions on the different mesh levels differ considerably. Figure 6(c) shows the centerline temperature profile for all of the prism meshs, and figure 6(d) shows the profiles for all of the unstructured hexahedral meshes. From figures 6(c) and 6(d) we

19

can clearly see the grid dependency of the centerline temperature profile. It is interesting to note that the prism solution is approaching a grid converged solution faster than the hexahedral mesh despite having less cells on meshes of the same level.

Figures 7(a) and 7(b) show the N_2 mass fraction profiles along the surface of the nozzle for level 4 and level 5 meshes, respectively. Again, we see little effect of grid convergence or the assumption of equilibrium mass fractions.

Figures 8(a) and 8(b) show the temperature profiles on the surface of the nozzle for level 4 and level 5 meshes, respectively. Unlike the centerline profiles which showed a strong grid dependency towards the center of the nozzle, the surface profiles show a fairly strong grid dependency at the inflow. We also can clearly see the effect of assuming equilibrium conditions at the inflow. As the grid is refined, the inflow is tending away from the equilibrium mass fractions, as expected. Again, we see that the prism meshes are capturing the trends earlier than the hexahedral solutions.

Ram II-c

During the late sixties a series of probes were flown in a velocity regime in which ionization would play an important role. The second series of tests, known as the Ram II-c experiments, have become a popular test case for modern CFD codes. During the later series of flights, water and electrophilic liquid [36] were injected into the plasma layer to reduce the free electron density level. However, only data for the flights without injection are available.

The geometry of the probes consisted of a sphere-cone configuration with a 15.24 cm nose radius and a 9 degree cone half angle. The probes were instrumented to measure electron density during the flight. Eight wire probes were located on the leading edge of the rake with the last probe extending approximately 7 cm into the plasma layer. Collectors were placed with their longitudinal axis at 46 degrees to the flow direction and biased with a constant negative voltage to collect ions.

The case considered in this report corresponds to a flight altitude of 61Km with free stream conditions: $T_\infty = 254K, U_\infty = 7650m/s$, and a Reynolds number based on the nose radius $R_{en} = 19,500$. These conditions correspond to a flight Mach number of 23.9. The chemistry model used to obtain the solutions is the air chemistry model described by Park [37]. The Park air chemistry model contains 7 species $(N_2, O_2, NO, NO^+, N, O, e^-)$ and 18 reactions.

Figures 9(a) and 9(b) show the level 2 and level 3 prism meshes used to obtain the unstructured solution. The computed Mach contours for the two meshes are shown in figures 10(a) and 10(b).

Figure 11 shows the electron number density on the surface of the probe for the unstructured prisms, structured hexahedrals and experimental data. On these meshes, both the structured hexahedral and the unstructured prism solutions overpredicted the electron number density on the aft portion of the body. It is worth noting that if the flowfield was initialized to the freestream Mach number that convergence problems for both the structured and unstructured codes were experienced. In this case, the shock wave forms on the body and moves outward into the flow field resulting in a severe transient which limited the time step. By initializing the flow to a low Mach number and enforcing

freestream conditions on the outer boundary, the shock moves inward towards the body, enabling a much higher Courant number.

Aeroassist Flight Experiment

A family of vehicles, known as aeroassist vehicles, are currently under design. These vehicles operate in the upper reaches of the atmosphere and at velocities higher than those encountered by typical reentry vehicles.

A class of these vehicles, known as aeroassist orbital transfer vehicles (AOTV), are being designed to transfer payloads from a low earth orbit to a high earth orbit and back. In returning, the vehicles velocity must be greatly reduced to the earth orbital velocity and achieve capture in low earth orbit. This reduction in velocity may be achieved by one of two methods, the use of retro rockets or by allowing aerodynamic drag forces to act on the vehicle. Studies indicate that fuel loads are lowered and therefore the payload may be increased using the second method. Because of the high altitude and high velocity, ground based facilities are not capable of reproducing these conditions. In order to better understand the physics of these problems, the AFE has been proposed by the National Aeronautics and Space Administration. The vehicle will be transported by the space shuttle and placed in a low earth orbit. The AFE will then be propelled into the atmosphere to simulate the velocity and trajectory of a return mission from geosynchronous orbit. The data obtained will then be used to validate current computational fluid dynamics codes which will be used in future AOTV designs.

The AFE will travel in the Earths upper atmosphere at velocities ranging from 7 to 10 km/s. At these conditions, chemical and thermal non-equilibrium effects are significant. The AFE project was designed to obtain critical flight data that will be used to validate hypersonic computational fluid dynamic codes. Two sets of solutions for the AFE were obtained. The first set of solutions corresponds to a free stream Mach number of 10. The Mach 10 case is significant because good experimental data exists for this problem. The second set of solutions is for a free stream Mach number of 31.7. In this case only code on code validations are available at this time.

Solutions to the AFE proved to be very stiff and difficult to obtain. The solutions presented here were obtained with the GM-Res time integration scheme. To further increase the efficiency, mesh sequencing was used on a series of meshes. A total of 5 meshes were generated in the process. Several views of the finest AFE mesh are shown in figure 12. The body of the AFE has been mirrored about the plane of symmetry to provide a full view of the proposed configuration. The mesh displayed in figure 12 contains approximately 106,000 cells and 202,000 faces.

The solution for the Mach 10 test case is presented in figure 13. This figure shows a comparison of the computed and experimental data for the pressure coefficient over the surface of the AFE in the plane of symmetry. Two sets of computed results are presented in this figure; the first set corresponds to a medium mesh of approximately 50,000 cells, and the second set corresponds to the fine mesh shown in figure 12. As can be seen from the figure, both sets of computed results compare favorably to the experimental data of J.R. Micol [38].

Results for the Mach 31.7 test case are presented in figure 14(a) through 14(d). The freestream conditions for this test case correspond to point 1 of the planned trajectory.

This corresponds to a free stream velocity of 9.818 Km/s, a mixture density of 1.542×10^{-5} kg/m^3, and a temperature of 195.3 K. The flow was assumed to be in chemical and thermal non-equilibrium. The freestream mass fractions were obtained using a standard air composition for N_2 and O_2. All other species were absent from the freestream. The solutions were obtained using the 7 species, 18 reaction Park air chemistry model [37] discussed earlier.

In figures 14(a) and 14(b), the electron number density and temperature are shown. The electron number density plot compares favorably to the solutions obtained by Greendyke, Gnoffo, and Lawrence [39]. In figures 14(c) and 14(d), contours of the O_2 and O species densities are shown. At these temperatures we would expect to see complete dissociation of O_2. This is clearly evident from this figure.

It should be pointed out that the assumptions in the thermo-chemical modeling implemented in the unstructured code are not entirely valid for this flow field. In addition, the grid for the Mach 31.7 case needs to be refined near the body of the vehicle. For the simulation of the high speed test case the mesh is far too coarse behind the shock to properly capture all of the physics of this complex flow field. However, despite the assumptions and poor quality of the mesh, the results are adequate. The effect of the assumptions is also seen for the Ram-IIc simulations shown in Applebaum [30] [40]

Analytic Forebody

The analytic forebody problem has been studied experimentally as well as numerically [34]. The problem represents the inviscid supersonic flow over the cockpit region of a high performance aircraft. The geometry consist of a cross section which develops smoothly from circular at the nose through a lobed analytic curve and back to circular at the aft section of the body. This case was chosen to test the k-exact reconstruction method in three dimensions. The solution was obtained using mesh sequencing on two meshes. The finer of the meshes is shown in figure 15. This mesh corresponds to a structured 31x31x41 mesh which has been subdivided into tetrahedral cells. Three views of the forebody are shown, clockwise from the top, they represent the surface of the forebody, exit plane, and symmetry plane. The mesh in figure 15 contains approximately 230,000 cells, 440,000 faces, and 40,000 nodes.

The freestream conditions for this problem are given by: $M_\infty = 1.7$, $\rho_\infty = 1.1774$ kg/m^3, $P_\infty = 101325$ N/m^2, and the angle of attack $\alpha = 0$. The solution was obtained using the k-exact reconstruction method for the inviscid fluxes. The inviscid fluxes were computed using the Roe flux difference splitting algorithm discussed earlier. The Runge-Kutta explicit time integration scheme was used to advance the solution in time. The solution on the coarse mesh required 11306 iterations to reduce the residual 6 orders. On a Cray YMP this required 17 minutes of CPU time. The finer solution was converged an additional 2 orders in 8306 iterations which required 1 hour and 46 minutes of Cray YMP time.

The solution to the forebody is shown in figures 16 and 17. In figure 16, the pressure contours are shown on the top and bottom planes of symmetry. In figure 17, the surface pressure distribution in the plane of symmetry is compared to experimental data [34]. As can be clearly seen, the results compare favorably to the experimental data. Note that in

the aft section of the forebody the predicted values are slightly lower than the experimental data. Papay [41] showed that for an inviscid solution to the analytic forebody this is typical. Papay also showed that solutions obtained with with an appropriate turbulence model provide better agreement in this region.

2-D Laminar Flat Plate

The two dimensional flow of a perfect gas over a one meter long flat plate at a freestream Mach number of 0.3 is presented in figure 18. The freestream temperature and density are 500 K and 0.03973 kg/m^3 respectively. The Reynolds number based on the length of the plate is 200,000 which is well within the valid range for laminar flow. The problem is aligned so that the plate runs along the x-axis and the y-axis is normal to the plate. To obtain the solution, a quadrilateral 21x41 mesh was converted to a triangular mesh by subdivided each quadrilateral into two triangular cells.

The boundary condition at the inflow fixes the total temperature and total pressure. The pressure is extrapolated from the interior, and the density and velocity are computed based on the extrapolated pressure and the specified total temperature and total pressure. The boundary condition at the outflow sets the pressure to the specified back pressure. All other flow quantities are extrapolated. The surface of the flat plate is modeled using a no-slip adiabatic boundary condition. This boundary condition extrapolates the species densities, pressure, and temperature from the first interior cell. The velocity components u, v, w are set to zero. For the top boundary, all values are extrapolated from the interior.

Figure 18 shows a comparison of the similarity profiles computed at the exit plane to those of Blasius. Two solutions are presented in this figure. One of the solutions was computed using the k-exact reconstruction method for the viscous flux. The other solution was obtained using the thin layer approximation. The solutions were obtained using the GMRES implicit time integration, along with a second order k-exact reconstruction for the inviscid fluxes.

Both solutions provide excellent results. The numerical boundary layer thickness is approximately 0.012 meters which compares favorably to the Blasius value of 0.0116.

2-D Turbulent Flat Plate

The solution presented in this section represents the two dimensional turbulent, supersonic flow over a one meter long flat plate. The conditions in the freestream correspond to $M_\infty = 2.244$, $T_\infty = 170K$, and $\rho_\infty = 0.4538 kg/m^3$. This corresponds to a Reynolds number of $2x10^7$. The solutions were obtained using the one equation Spalart and Allmaras model discussed earlier. The turbulence model working variable was initialized to ten times the freestream laminar viscosity. The k-exact reconstruction algorithm was used to determine the viscous and inviscid fluxes. The wall boundary condition extrapolates the density, pressure, and temperature and sets the velocity components to zero. This corresponds to an adiabatic wall boundary. To obtain the solution, a 41x81 quadrilateral mesh was converted to a triangular mesh. This was accomplished by subdividing each quadrilateral cell into two triangular cells. The solution was advanced in time using the Runge-Kutta explicit time integration scheme. The solution required 59853 iterations to converge the solution 6 orders. On a Cray YMP this required approximately 23 minutes.

23

Figure 19 compares the unstructured solution at the exit plane to the analytic law of the wall plot. The analytical solution was obtained using the coefficients developed by Clauser [35]. Using these coefficients, the equation for the log region is given by

$$u^+ = 5.6 \log(y^+) + 4.9$$

In this figure, the frictional velocity u^* was taken to be constant throughout the boundary layer. The value of the frictional velocity was obtained from

$$u^* = \sqrt{\frac{\tau_w}{\rho_w}}$$

The wall shear stress was evaluated using the vorticity at the first cell off the wall.

Conclusions

A method for the solution to the Navier Stokes equations with a generalized thermo-chemical model and one equation turbulence model on unstructured meshes was presented. In addition a simple method for the k-exact reconstruction was reviewed. Several test cases were presented to test the efficiency of the viscous and thermo-chemical modeling. From the test cases, it was seen that the current methodology produces accurate results for the solutions presented.

Future Work

The aim of our generalized solution development program is to be able to accurately and efficiently solve the Navier Stokes equations on unstructured meshes with both equilibrium and non-equilibrium chemistry and thermodynamics. Building on this goal it is our hope to implement more turbulence models into the unstructured flow solver. Extensive validation of the flow solver is required.

Acknowledgements

References

1. Walters, R. W., Cinnella, P., Slack, D. C., and Halt, D., "Characteristic-Based Algorithms for Flows in Thermo-Chemical Nonequilibrium", AIAA 90-0393, January, 1990.
2. Drummond, J. P., Rogers, R. C., and Hussainni, M. Y., "A Detailed Numerical Model of a Supersonic Reacting Mixing Layer", AIAA/ASME/SAE/ ASEE 22nd Joint Propulsion Conference, 1986.
3. Grossman, B., and Cinnella, P., "The Development of Flux-Split Algorithms for Flows with Non-Equilibrium Thermodynamics and Chemical Reactions", AIAA Paper No. 88-0511, 1988.

4. Harten, A., Lax, P.D. and Van Leer, B., "On Upstream Differencing and Godunov-Type Schemes for Hyperbolic Conservation Laws", SIAM Review, Vol. 25, No. 1, 1983.

5. Roe, P.L., "Characteristic Based Schemes for the Euler Equations", *Annual Review of Fluid Mechanics*, Vol. 18, 1986.

6. Vinokur, M. and Liu, Y. "Equilibrium Gas Flow Computations II: An Analysis of Numerical Formulations of Conversation Laws", AIAA Paper No. 80-0127, 1988.

7. Liou, M.S., Van Leer, B. and Shuen, J.S, "Splitting of Inviscid Fluxes for Real Gases", *Journal of Computational Physics*, Vol. 74, 1988.

8. Glaister, P., "An Approximate Linearised Riemann Solver for the Euler Equations for Real Gases", *Journal of Computational Physics*, Vol. 74, 1988.

9. Grossman, B. and Walters, R.W., "Flux-Split Algorithms for the Multidimensional Euler Equations with Real Gases", *Computers and Fluids*, Vol 17, No 1, 1989.

10. Liu, Y., and Vinokur, M.,"Nonequilibrium Flow Computations I: An Analysis of Numerical Formulations of Conservation Laws", NASA CR 177489, 1988.

11. Candler, G.V. and MacCormack, R.W., "The Computation of Hypersonic Ionized Flows in Chemical and Thermal Nonequilibrium", AIAA Paper No. 88-0511, 1988.

12. Grossman, B. and Cinnella, P., "The Development of Flux-Split Algorithms for Flows with Non-Equilibrium Thermodynamics and Chemical Reactions", AIAA Paper No. 88-3595-CP, 1988.

13. Grossman, B., Cinnella, P., and Garrett, J., "A Survey of Upwind Methods for Flows with Equilibrium Chemistry and Thermodynamics", AIAA Paper No. 89-1653, 1989.

14. Wada, Y., Kubota, H., Ogawa, S. and Ishiguro, T., "A Generalized Roe's Approximate Riemann Solver for Chemically Reacting Flows", AIAA Paper No. 89-0202, 1989. SIAM Journal of Numerical Analysis, Vol. 21, No. 5, 1984.

15. Cinnella, P., and Grossman, B., "Upwind Techniques for Flows with Multiple Translational Temperatures", AIAA Paper No. 90-1660, 1990.

16. Steger, J. L., and Warming, R. F., "Flux Vector Splitting of the Inviscid Gas-Dynamic Equations with Applications to Finite Difference Methods", *Journal of Computational Physics*, Vol. 40, 1981.

17. Van Leer, B., "Flux vector Splitting for the Euler equations", in *Lecture Notes in Physics*, Vol. 170, ISBN 0-387-11948-5, Springer- Verlag, 1982.

18. Roe, P.L., "Approximate Riemann Solvers, Parameter Vectors, and Difference Schemes", *Journal of Computational Physics*, Vol. 43, 1981.

19. Vincenti, W. G. and Kruger, C. H. Jr., *Introduction to Physical Gas Dynamics*, ISBN 0-88275-309-6, Robert E. Krieger, 1965.

20. Barth, T.J., and Jespersen, D.C., "The Design and Application of Upwind Schemes on Unstructured Meshes", AIAA 89-0366, January, 1989.

21. Frink, N.T., Parikh, P., and Pirzadeh, S., "A Fast Upwind Solver for the Euler Equations on Three Dimensional Unstructured Meshes", AIAA 91-0102, January, 1991.

22. Barth, T.J., and Frederickson, P.O., "Higher Order Solution of the Euler Equations on Unstructured Grids Using Quadratic Reconstruction", AIAA 90-0013, January, 1990.

23. Mitchell, C. R., and Walters, R. W., "K-Exact Reconstruction for the Navier Stokes Equations on Arbitrary Grids", AIAA Paper No. 93-0536, 1993

24. Blottner, F. G., Johnson, M. and Ellis, M., "Chemically Reacting Viscous Flow Program for Multi-Component Gas Mixtures", Sandia Laboratories SC-RR-70-754, 1971.

25. Wilke, C. R., "A Viscosity Equation for Gas Mixtures", *The Journal of Chemical Physics*, Vol. 18, No. 4, 1950

26. Carpenter, M., "A Generalized Chemistry Version of SPARK", NASA CR 4196, 1988

27. Millikan, R. C., and White, D. R., "Systematics of Vibrational Relaxation", *The Journal of Chemical Physics*, Vol. 39, No. 12, 1963

28. McBride, B. J., Heimel, S., Ehlers, J. G. and Gordon, S., "Thermodynamic Properties to 6000K for 210 Substances Involving the First 18 Elements", NASA SP-3001, 1963.

29. Spalart, P.R. and Allmaras, S. R., "A One-Equation Turbulence Model for Aerodynamic Flows", AIAA 92-0439, January, 1992.

30. Applebaum, M. P., *Unstructured Technology for High Speed Flow Simulations*, PhD thesis, Virginia Polytechnic Institute and State University, Blacksburg, Virginia, Dec. 1994.

31. Saad, Y. and Schultz, M.H., "GMRES: A Generalized Minimum Residual Algorithm for Solving Nonsymmetric Linear System", SIAM J. Sci Stat. Comp., Vol. 7, No. 3, 1986, pp.856-869.

32. Wigton, L. B., Yu, N. J., and Young, D. P., "GMRES Acceleration of Computational Fluid Dynamics Codes", AIAA 85-1494, 1985.

33. Venkatakrishnan, V. and Mavriplis, D. J., "Implicit Solvers for Unstructured Meshes", ICASE Report 91-40, May 1991.

34. Townsend, J. C., Howell, D. T., Collins, I. K. and Hayes, C., "Surface Pressure Data on a Series of Analytic Forebodies at Mach Numbers from 1.70 to 4.50 and Combined Angles of Attack and Sideslip", NASA TM-80062, June, 1979.

35. Schetz, J. A., *Foundations of Boundary Layer Theory for Momentum, Heat, and Mass Transfer*, Prentice-Hall, ISBN 0-13-329334-4, 1984.

36. Kang, S. W., and Dunn, M. G., "Theoretical and Measured Electron-Density Distributions for the RAM Vehicle at High Altitudes", AIAA-72-689, 1972.

37. Park, C., "On Convergence of Computation of Chemically Reacting Flows", AIAA-85-0247, 1985.

38. Micol, J.R., "Experimental and Predicted Pressure and Heating Distributions for an Aeroassist Flight Experiment Vehicle in Air at Mach 10", AIAA-89-1731, AIAA 24th Thermophysics Conference, Buffalo, NY, June 1989.

39. Gnoffo, P.A., Lawrence, R.W., and Greendyke, R.B., "Electron Number Density Profiles for the Aeroassist Flight Experiment", AIAA Paper No. 92-0804, January, 1992.

40. Applebaum, M. P., Mitchell, C. R., Walters, R. W. and McGrory, W. D., "Application of Thermo-Chemical Models on Unstructured Meshes", AIAA 93-0895, January, 1993.

41. Papay, M. L., *A General Reverse Design Procedure for Aerodynamic Bodies*, PhD thesis, Virginia Polytechnic Institute and State University, Blacksburg, Virginia, May, 1994.
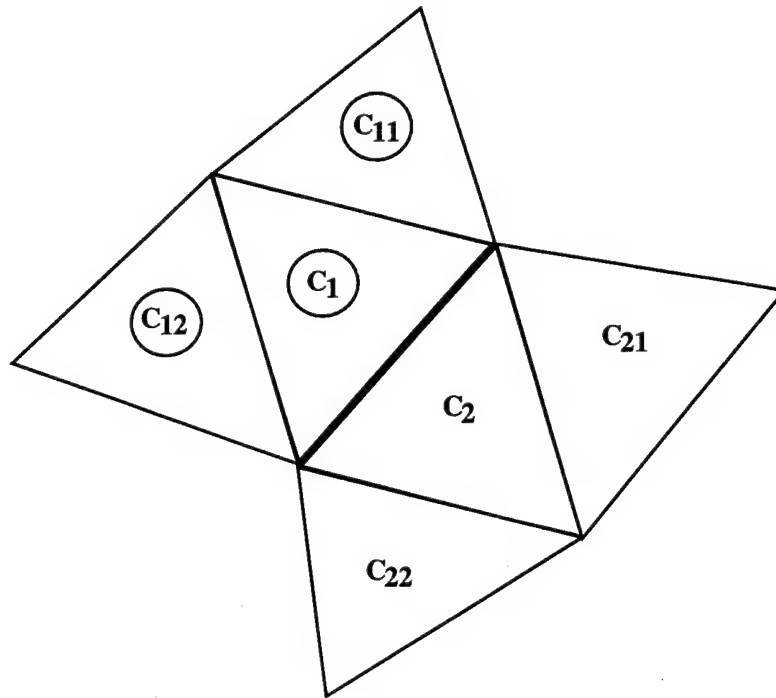
Figure 1(a): Upwind Stencil Selection
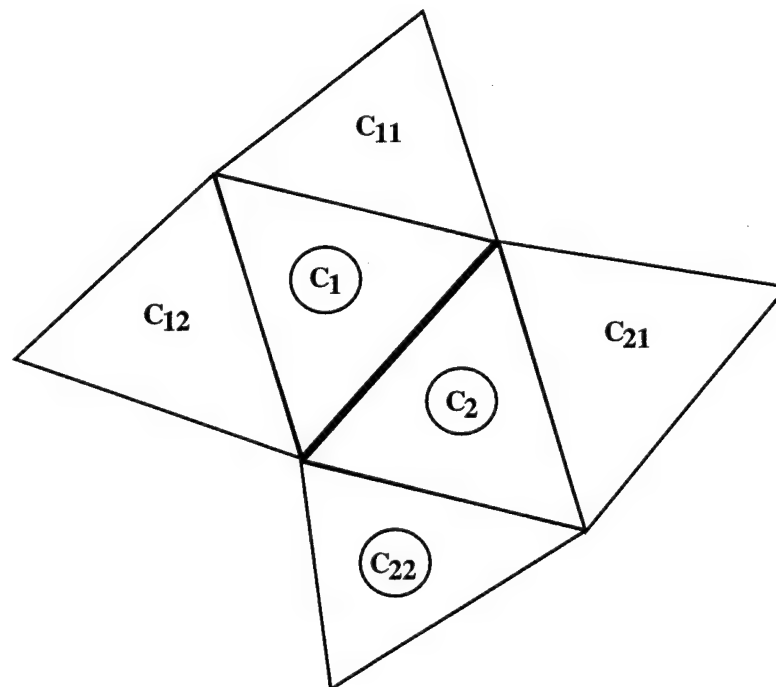
Figure 1(b): Viscous Stencil Selection

27
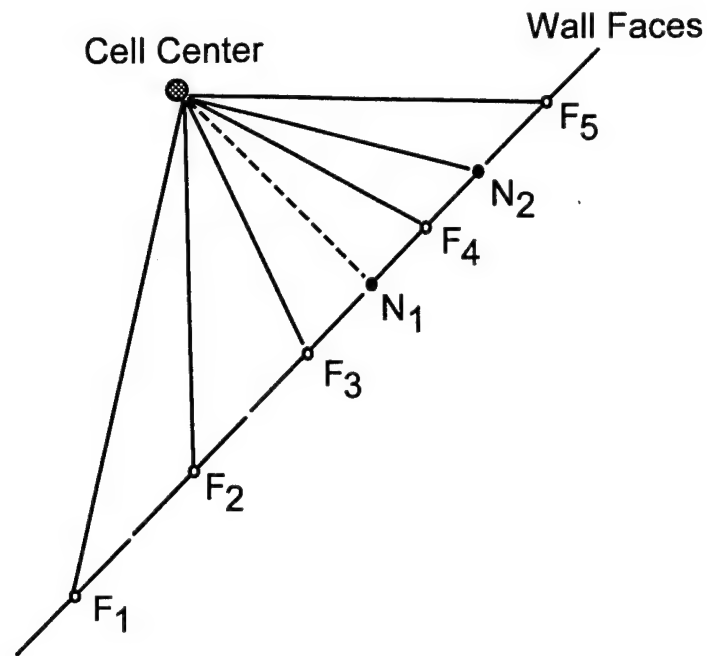
Figure 2: Turbulence model distance function pseudo-algorithm
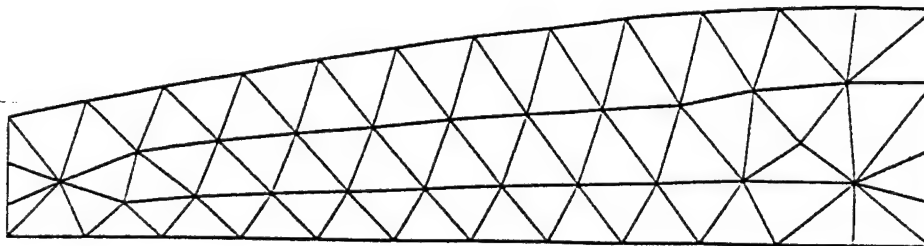
Figure 3(a): Air nozzle level 01 prism mesh
250 cells, 271 faces, 106 nodes
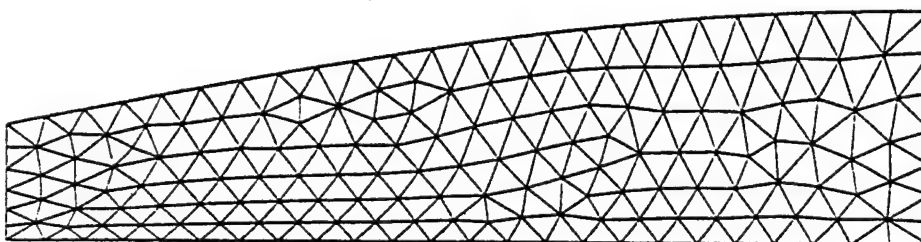
Figure 3(b): Air nozzle level 02 prism mesh
958 cells, 1077 faces, 362 nodes
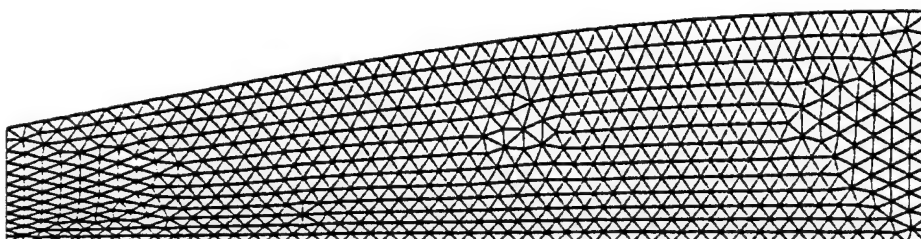
Figure 3(c): Air nozzle level 03 prism mesh
3742 cells, 4287 faces, 1328 nodes
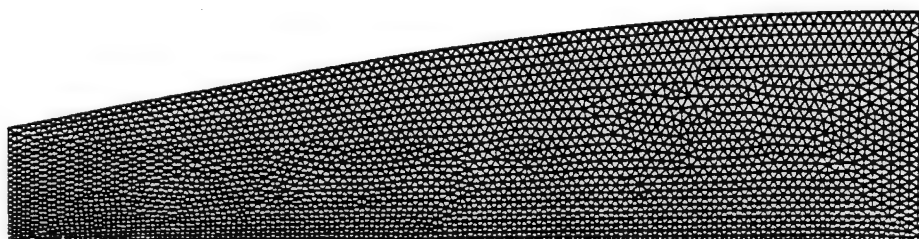
Figure 3(d): Air nozzle level 04 prism mesh
14798 cells, 17109 faces, 5090 nodes
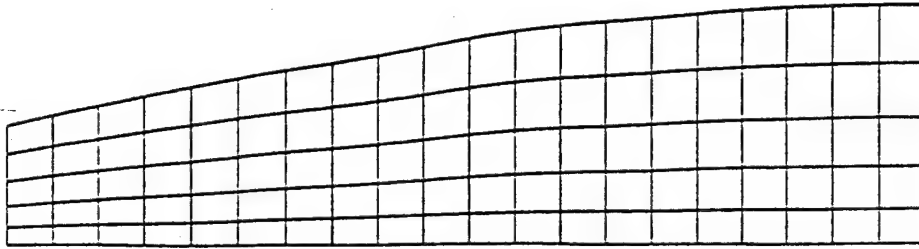
Figure 4(a): Air nozzle level 01 hexahedral mesh
350 cells, 425 faces, 252 nodes
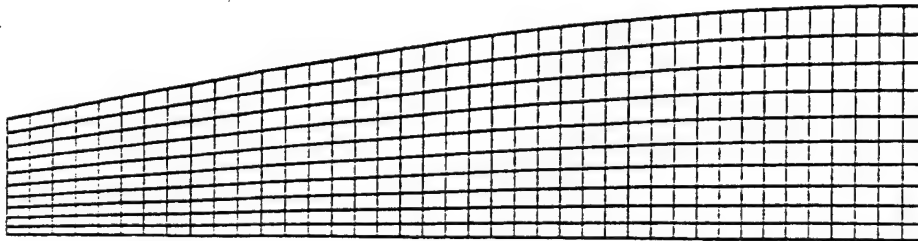
Figure 4(b): Air nozzle level 02 hexahedral mesh
1300 cells, 1650 faces, 902 nodes
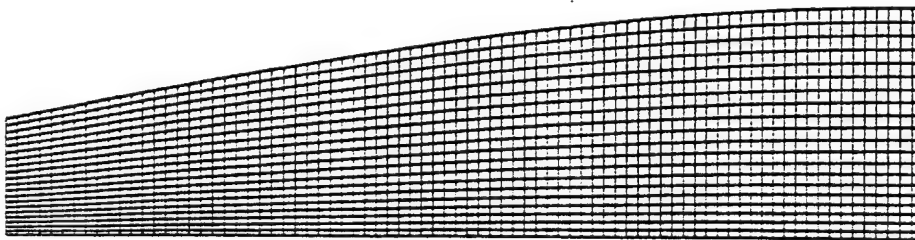
Figure 4(c): Air nozzle level 03 hexahedral mesh
5000 cells, 6500 faces, 3402 nodes
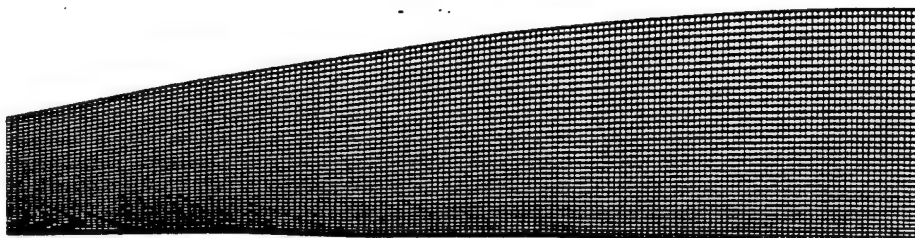
Figure 4(d): Air nozzle level 04 hexahedral mesh
19600 cells, 25800 faces, 13202 nodes
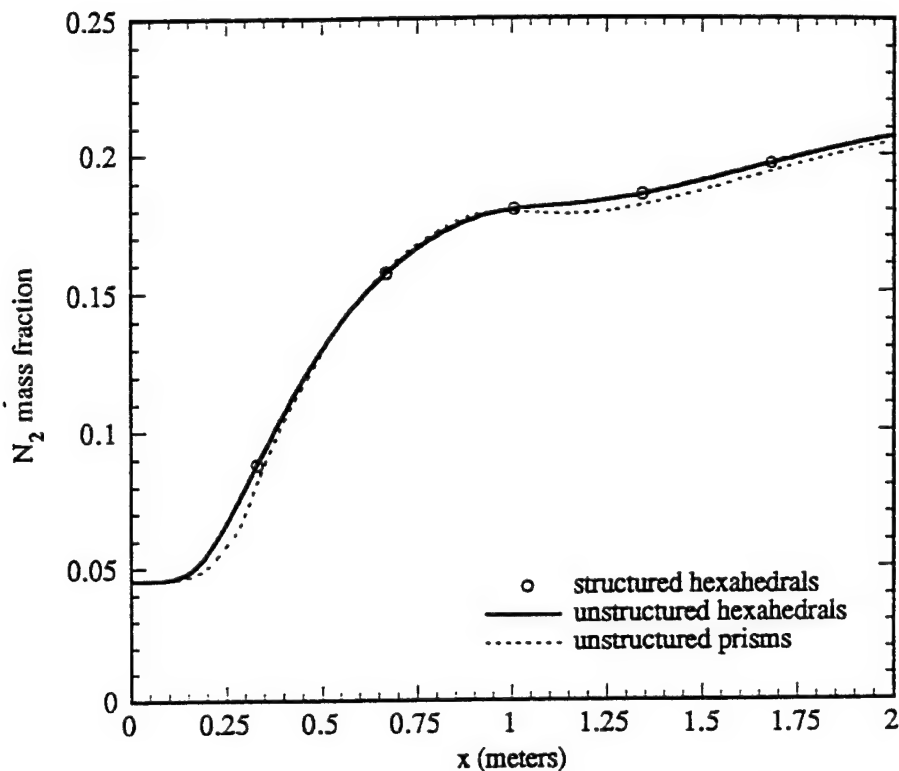
Figure 5(a): Air nozzle centerline N_2 mass fraction
profile for level 04 grids
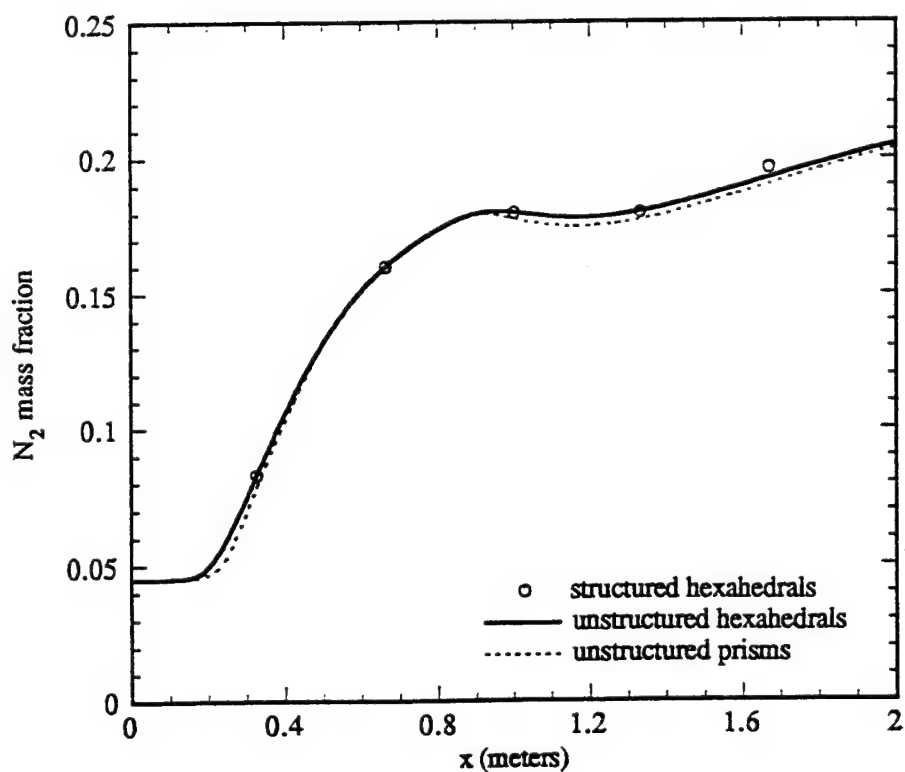
Figure 5(b): Air nozzle centerline N_2 mass fraction
profile for level 05 grids
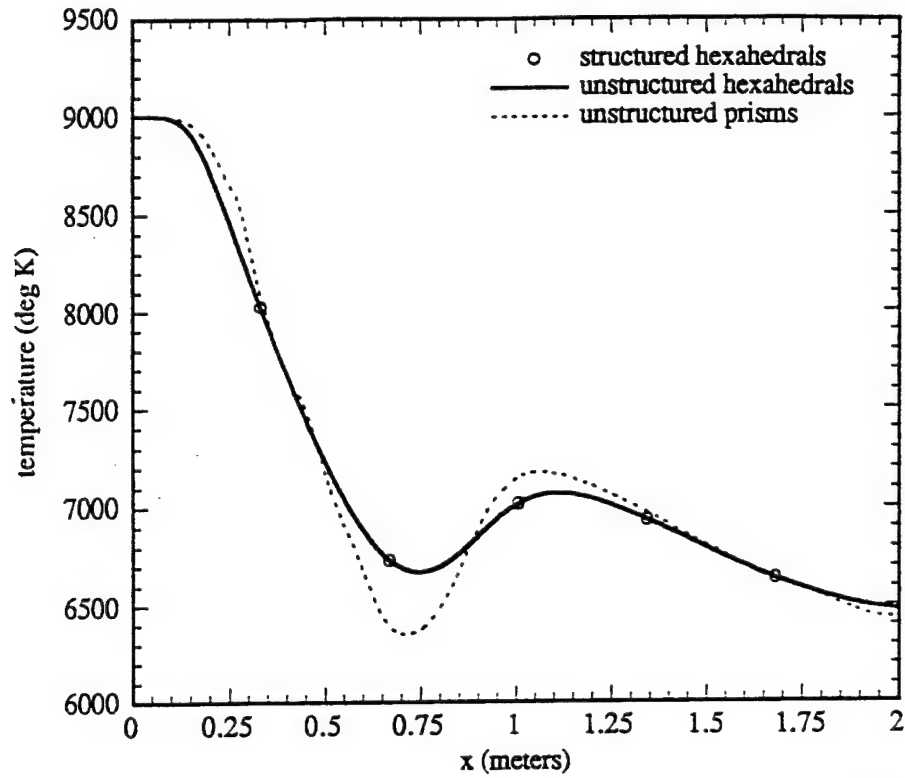
Figure 6(a): Air nozzle centerline temperature profile
for level 04 grids
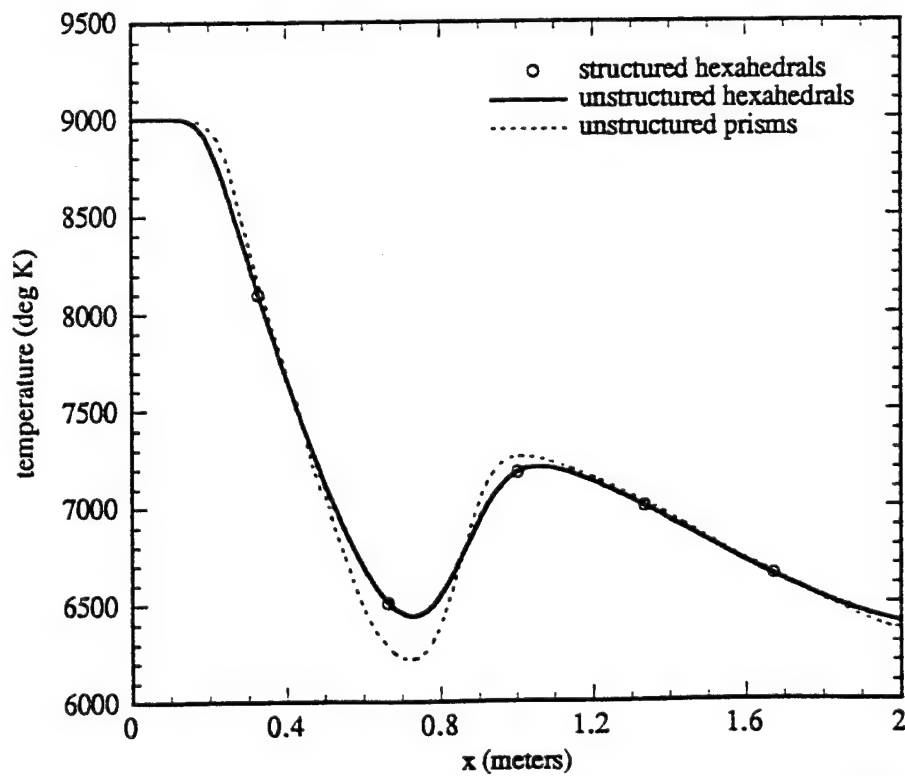
Figure 6(b): Air nozzle centerline temperature profile
for level 05 grids
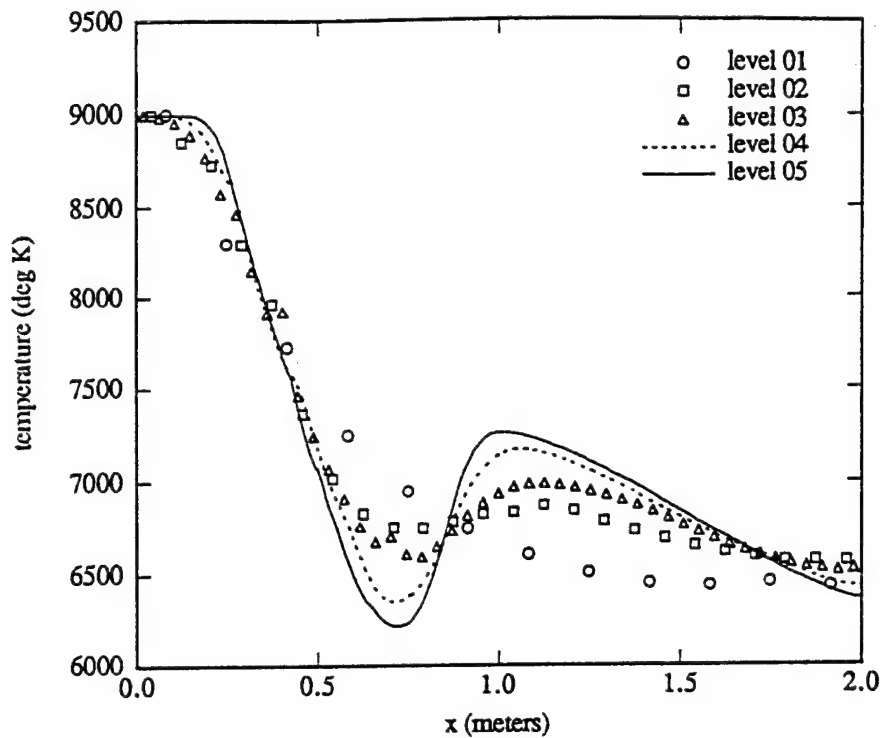
Figure 6(c): Air nozzle centerline temperature profile
for prism grids (all levels)
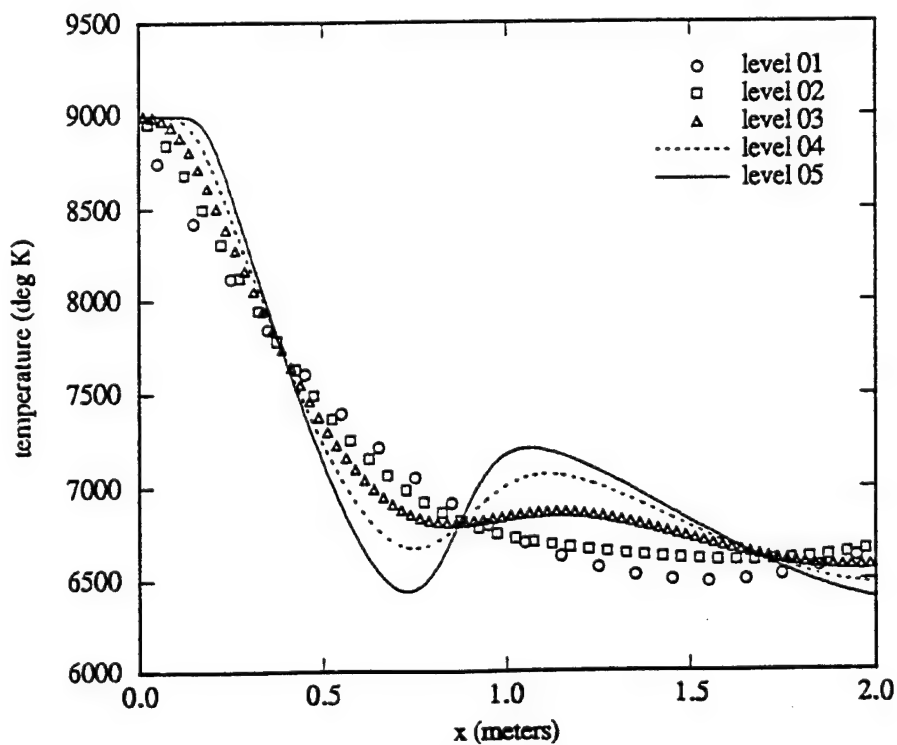
Figure 6(d): Air nozzle centerline temperature profile
for hexahedral grids (all levels)

33
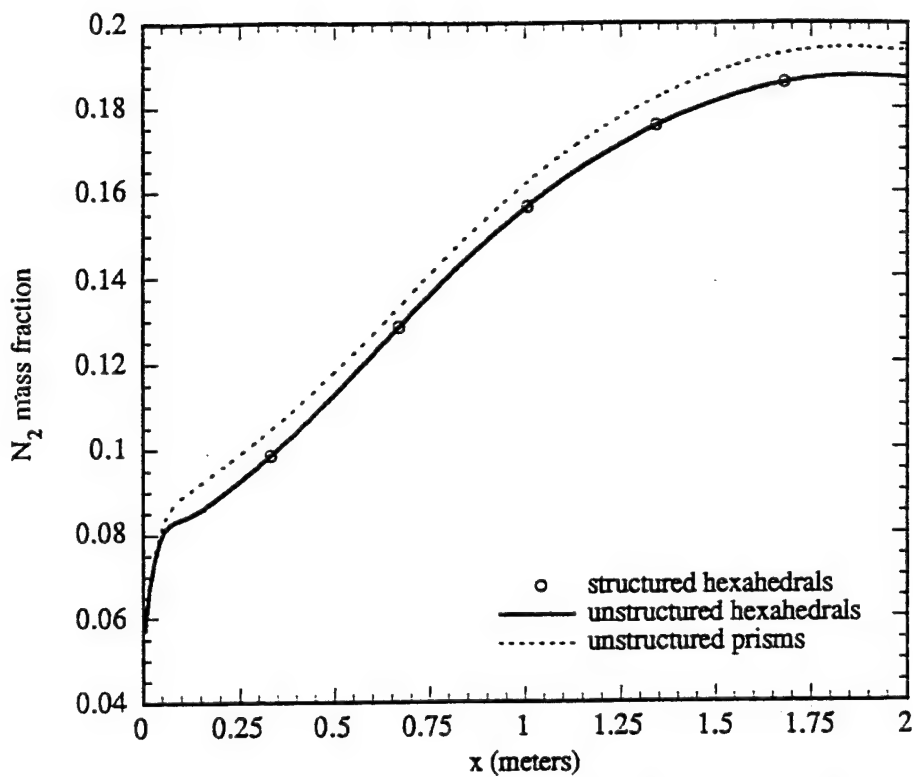
Figure 7(a): Air nozzle surface N_2 mass fraction
profile for level 04 grids
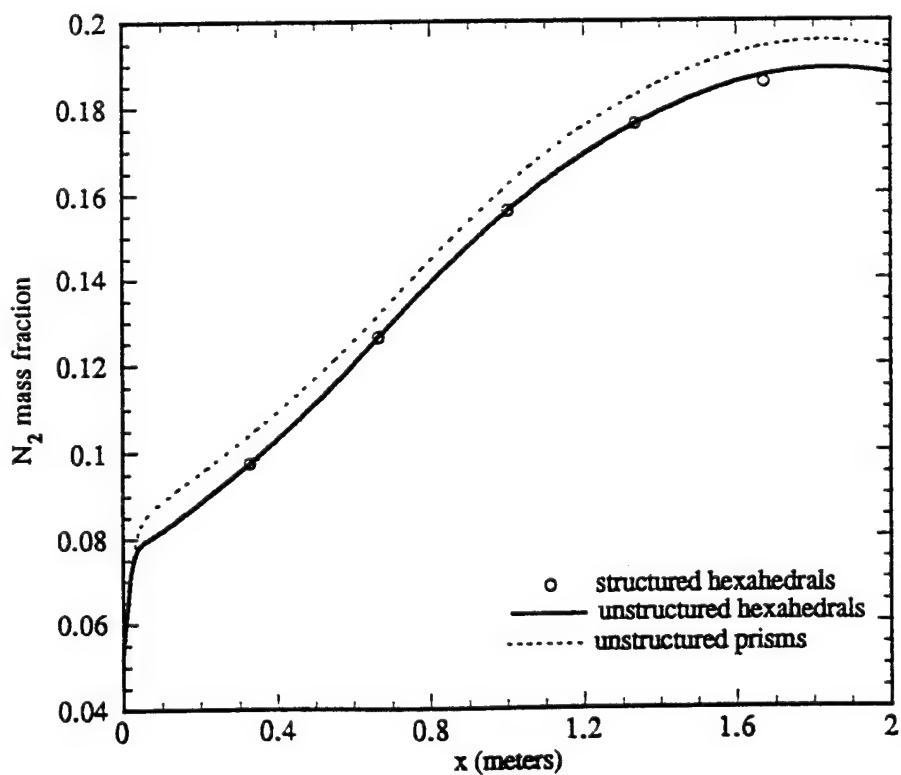
Figure 7(b): Air nozzle surface N_2 mass fraction
profile for level 05 grids
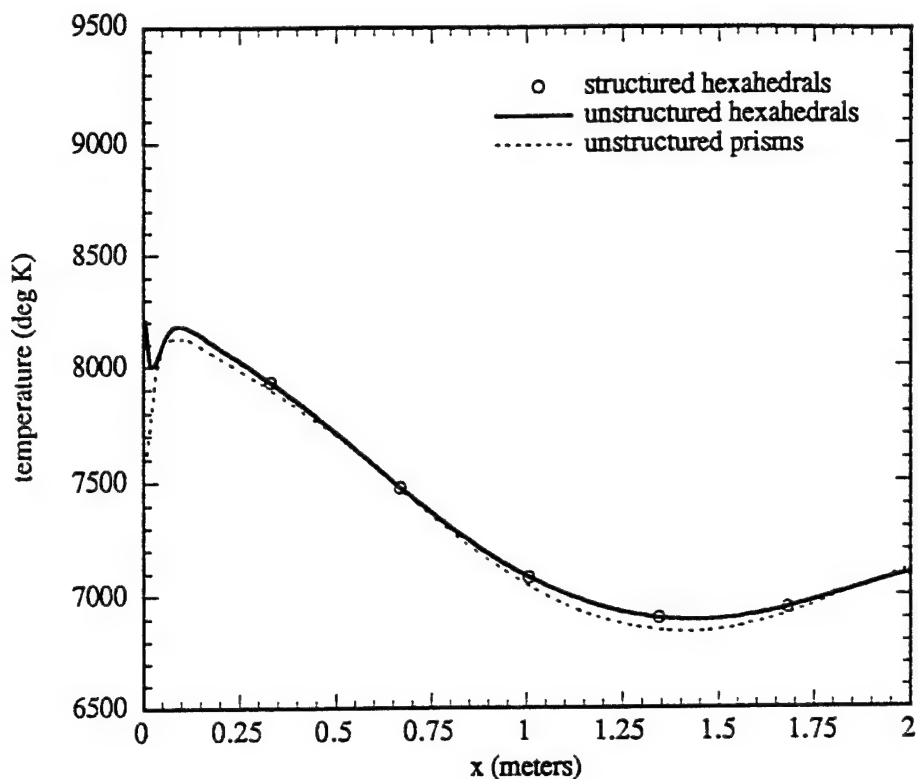
Figure 8(a): Air nozzle surface temperature profile for
level 04 grids
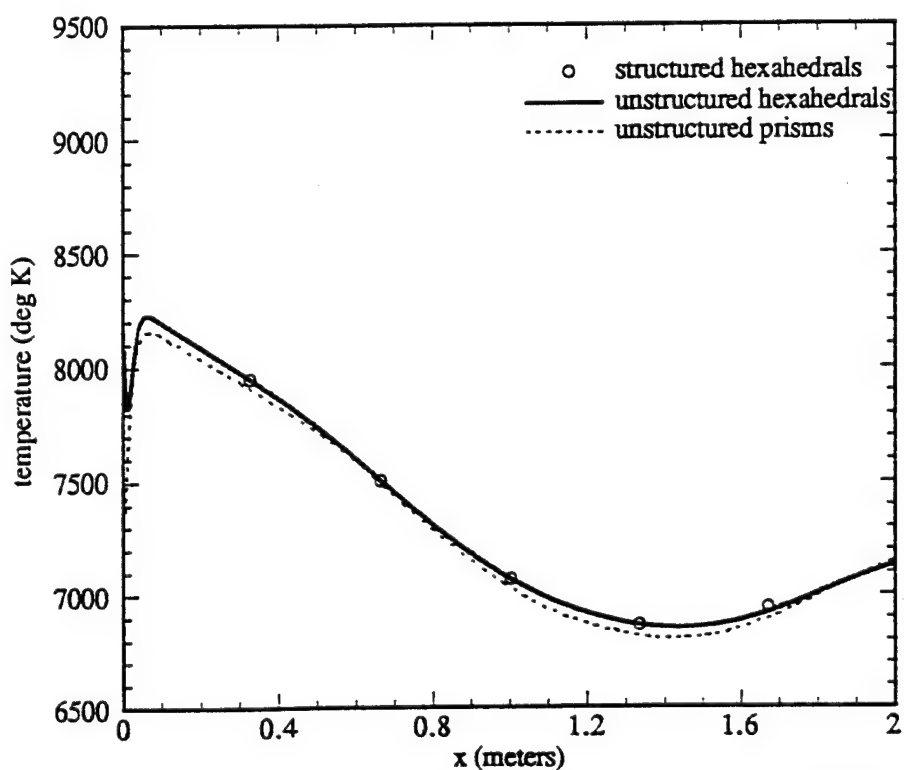
Figure 8(b): Air nozzle surface temperature profile for
level 05 grids
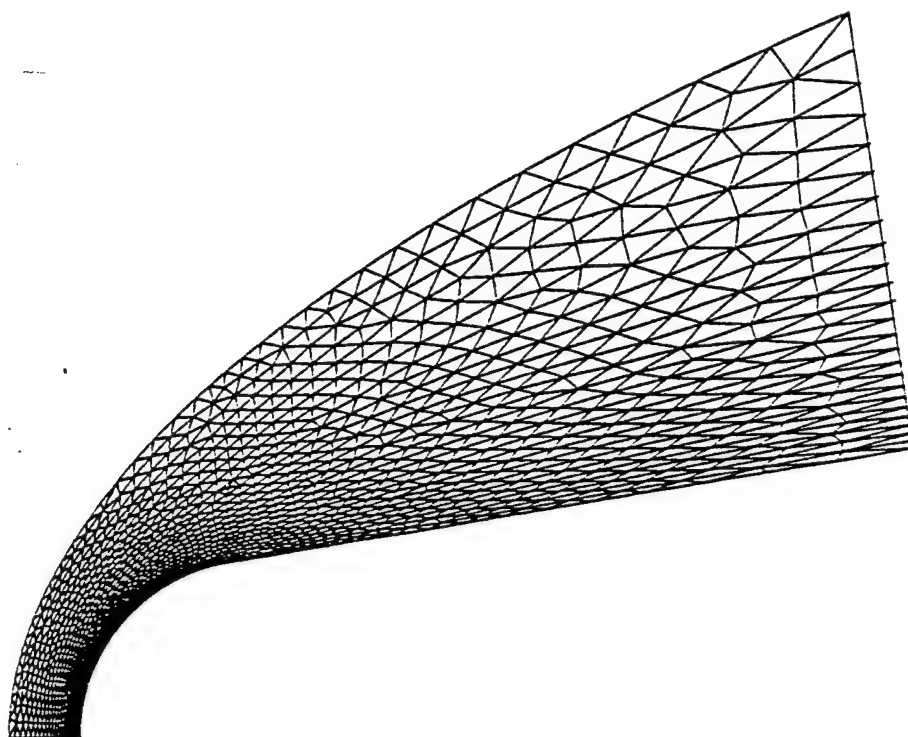
Figure 9(a): Ram II-C level 02 prism mesh
5688 cells, 6558 faces, 1976 nodes
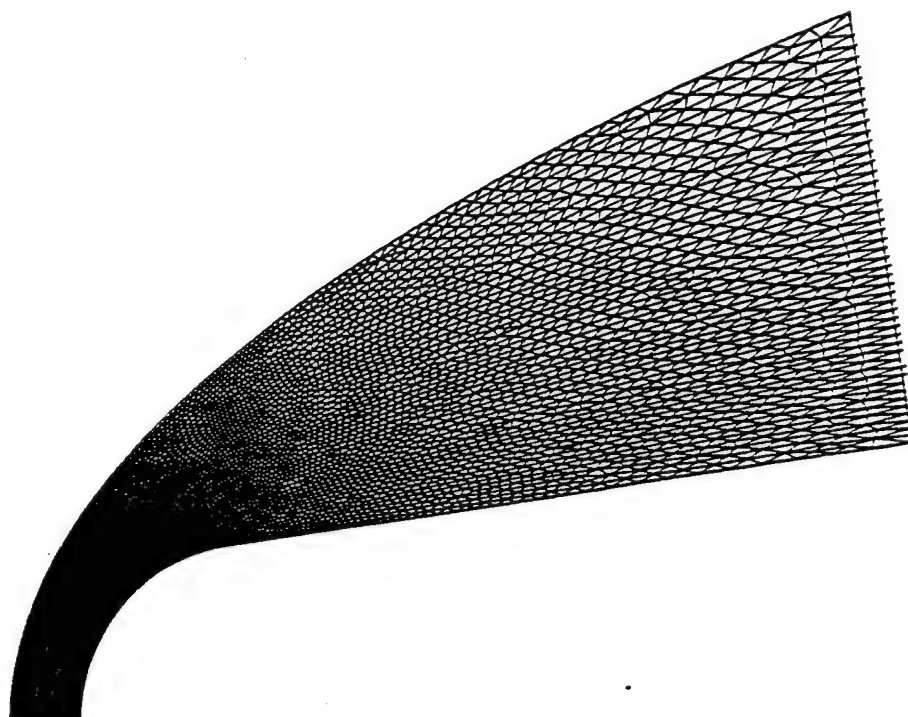
Figure 9(b): Ram II-C level 03 prism mesh
21686 cells, 25145 faces, 7386 nodes

36
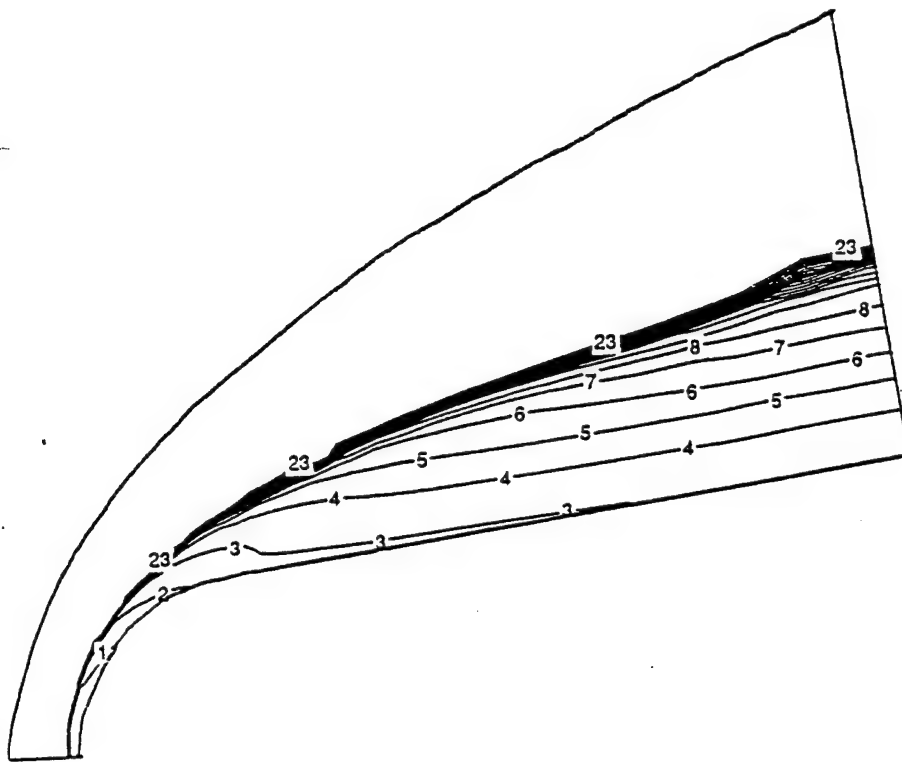
Figure 10(a): Ram II-C Mach contours on level 02 mesh
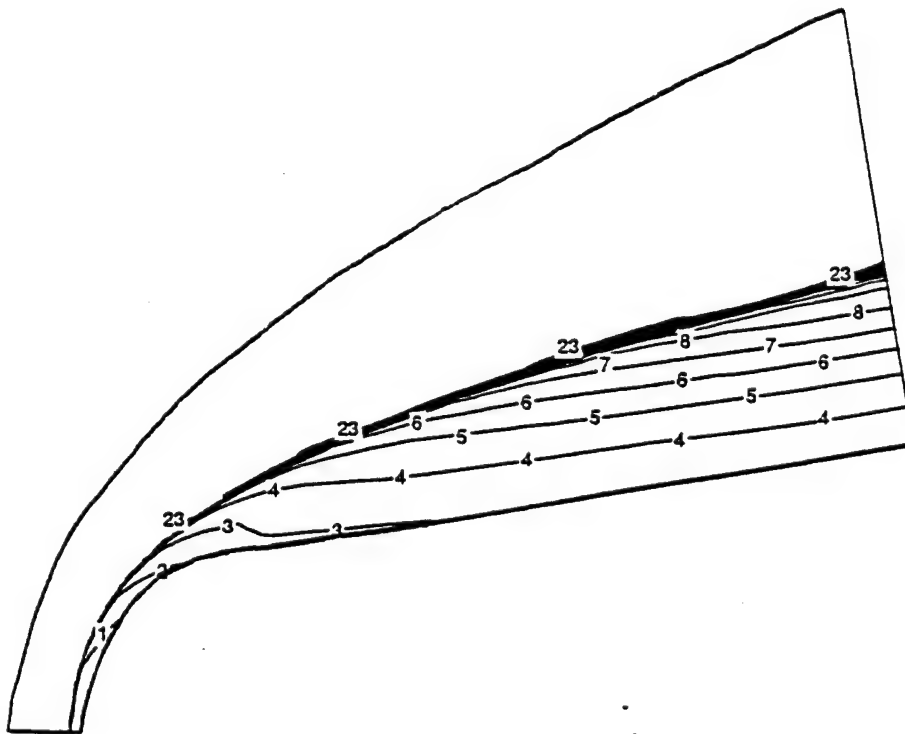
Figure 10(b): Ram II-C Mach contours on level 03 mesh
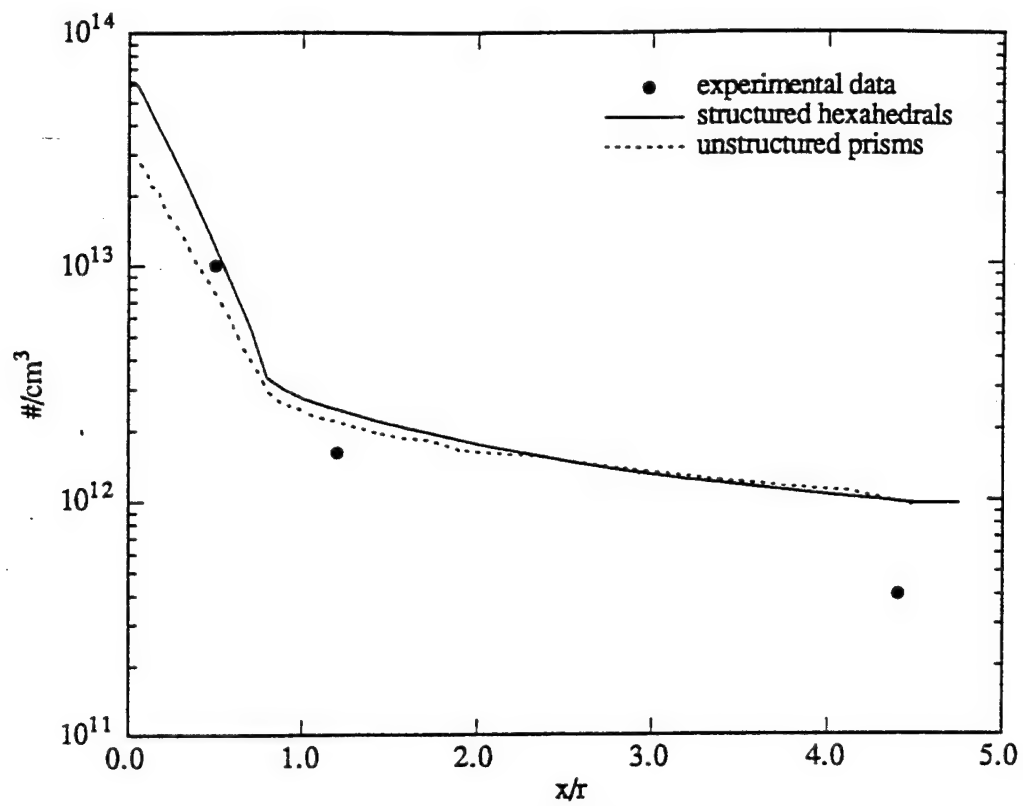
Figure 11: Ram II-C surface electron number density
at 61Km
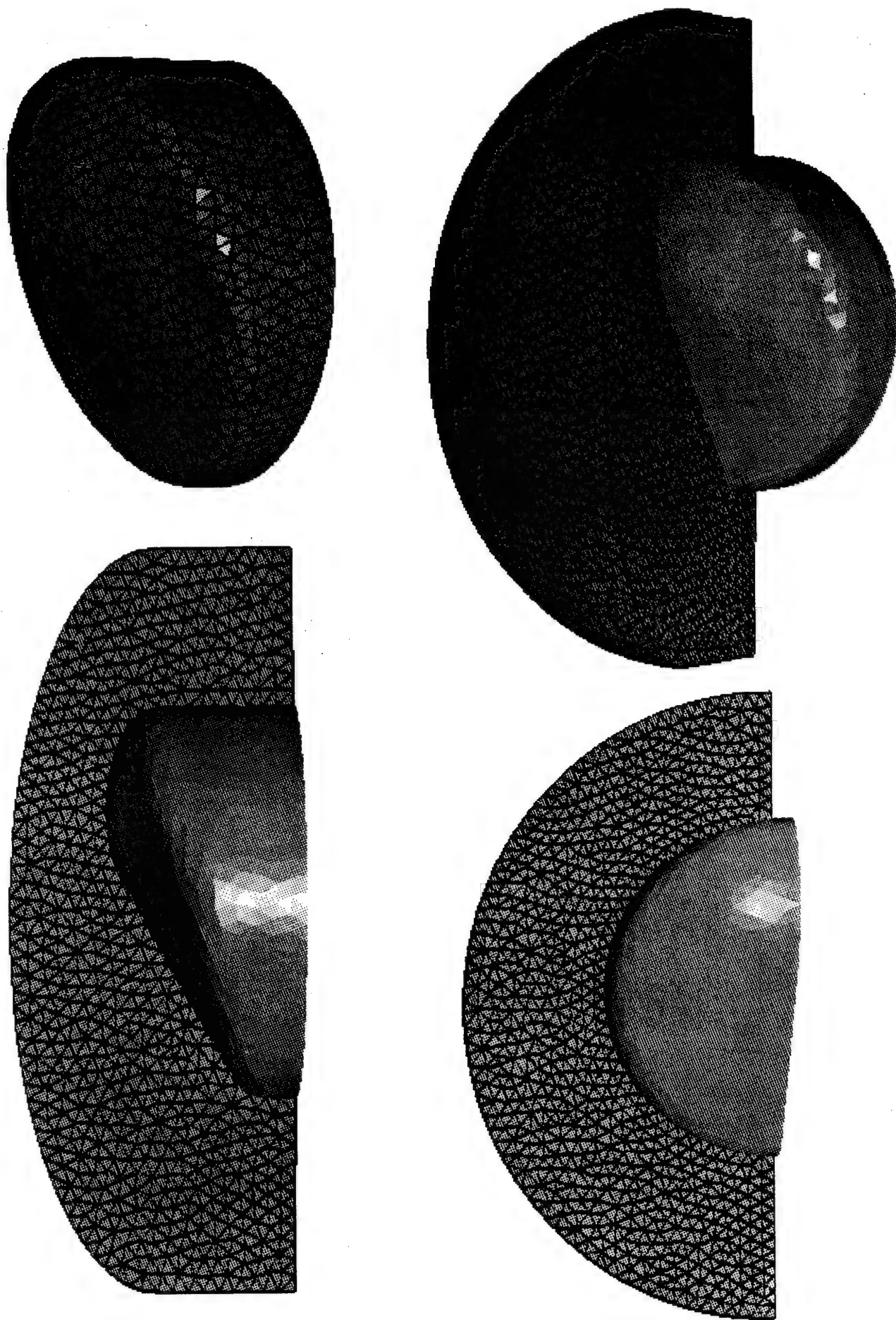
Figure 12: Several views of the Aeroassist Flight Experiment mesh.
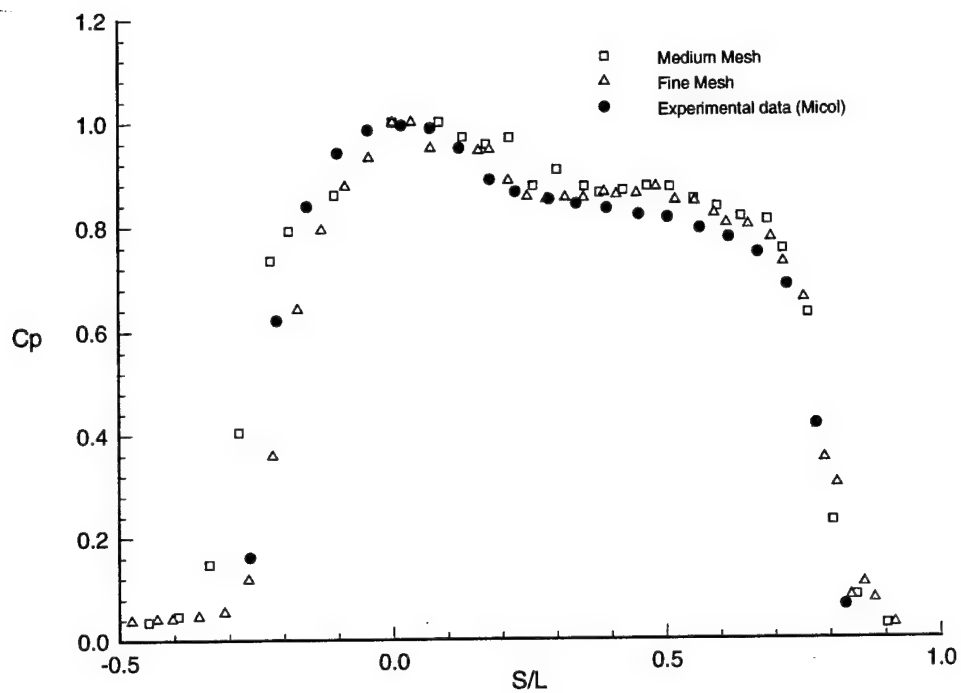
Fig 13: Pressure distribution on surface
of AFE for Mach 10 test case
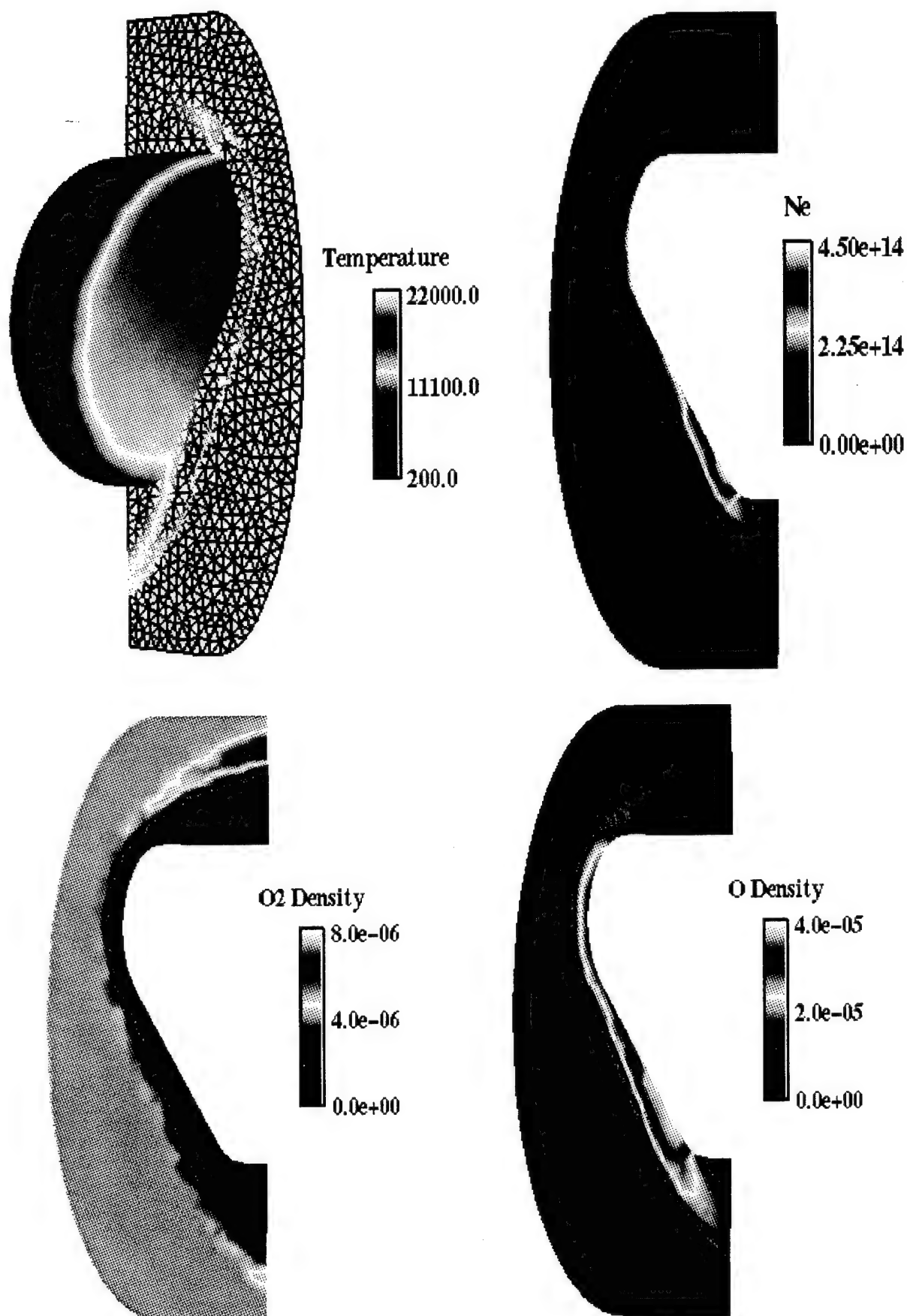
Figure 14: AFE solutions for the Mach 31.7 case: Clockwise from top, Temperature,
electron density, O2 density & O density profiles
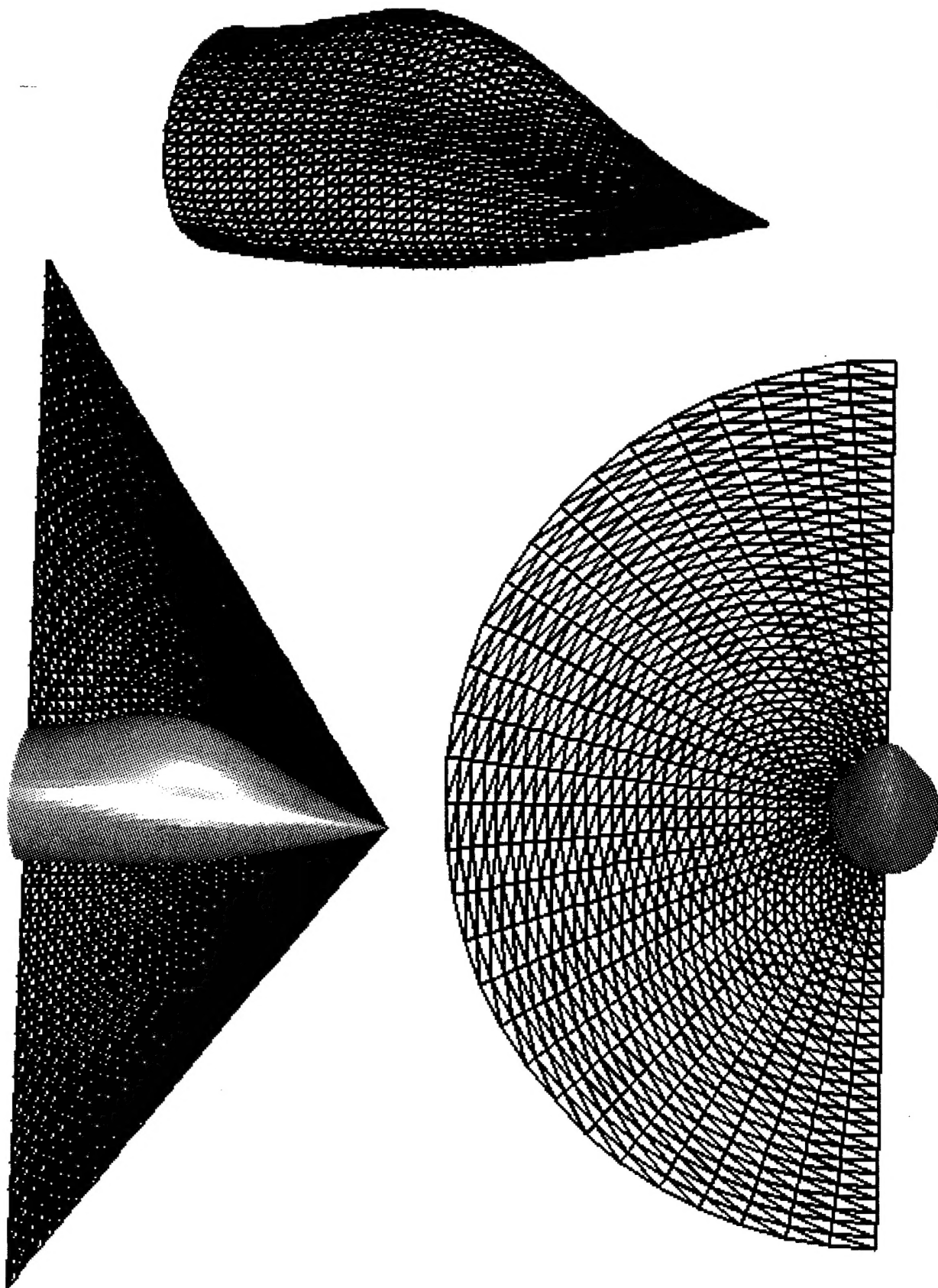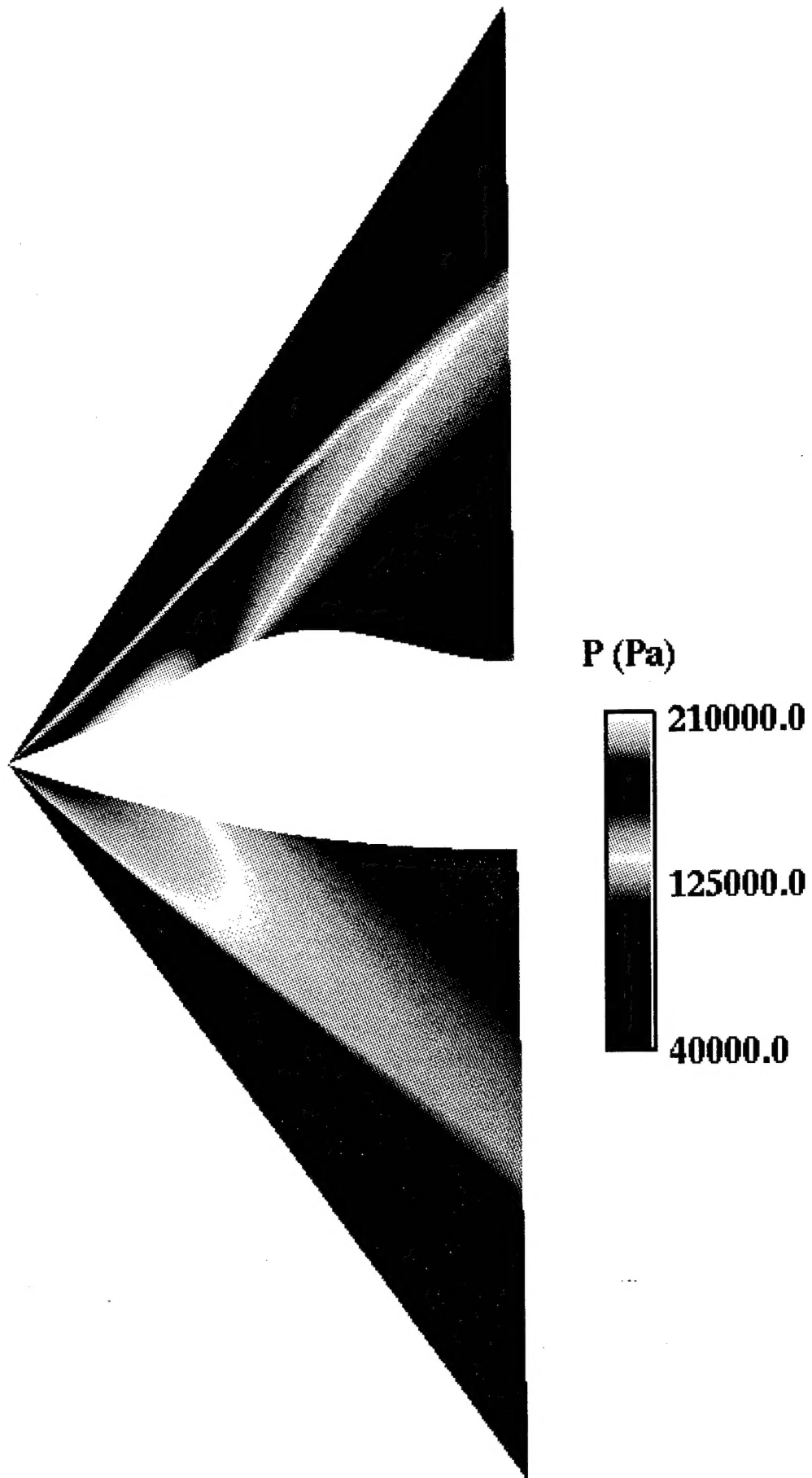
Figure 15: Several views of the analytic forebody mesh.

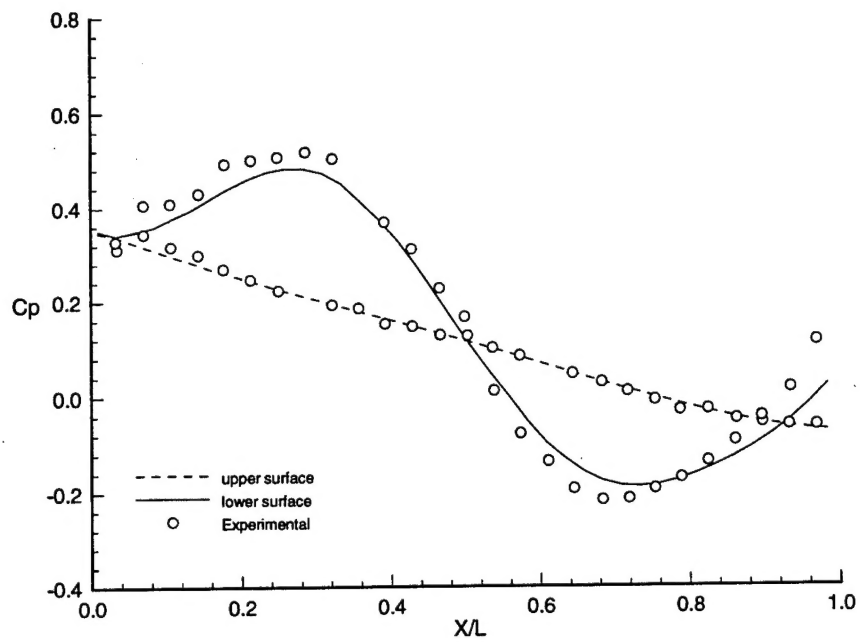Figure16: Analytic forebody pressure contours in symmetry plane

Fig 17: Analytic Forebody surface pressure distribution
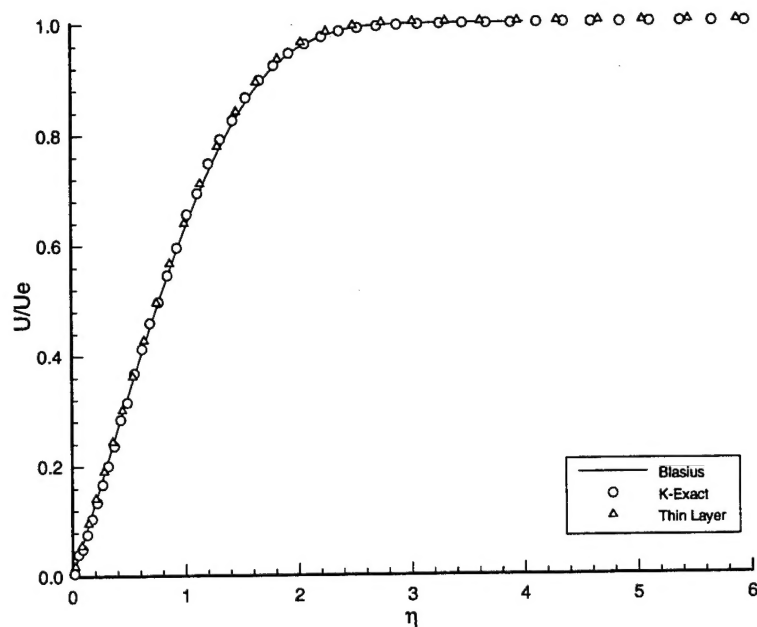in symmetry plane

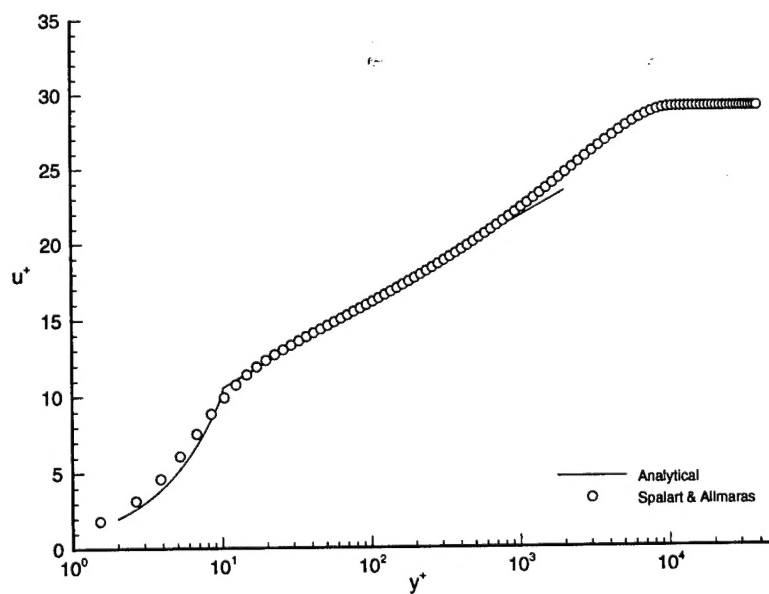Fig 18: Similarity profiles for subsonic
laminar flat plate

Fig 19: Wall law plot for the supersonic
flat plate